 doi:10.20944/preprints202102.0495.v1

Efficient visible active ternary Bi_2MoO_6-rGO-TiO_2 composite material for photodecomposition of ofloxacin

Annamalai Raja*, Namgyu Son, Misook Kang*

Department of Chemistry, College of Natural Sciences, Yeungnam University, Gyeongsan, Gyeongbuk 38541, Republic of Korea

*Corresponding authors: rajaannamalai@yu.ac.kr, rajaannamalai88@gmail.com (A. Raja), mskang@ynu.ac.kr (Misook Kang),

Abstract

The ternary Bi_2MoO_6-reduced graphene oxide (rGO)-TiO_2 catalyst were synthesized using a simple hydrothermal method. The improvement of the photocatalytic decomposition efficiency of Bi_2MoO_6-rGO-TiO_2 composite is 92.3% than the pure and binary photocatalyst. The effects of operational parameters like catalyst ratio, the different catalyst, different ratio rGO and different pH, have been analyzed. As prepared ternary photocatalyst is low Photoluminescence and high photocurrent density responsible, it exhibited that photon-induced electron and hole-recombination were suppressed and also charged separation is effective. The present study to shows the rGO is an excellent electron transfer performance and enhanced the photocatalytic reaction stability.

Keywords: Visible light; Ofloxacin; Reduced graphene oxide; photocatalytic degradation; photocurrent density.

Preprints (www.preprints.org) | NOT PEER-REVIEWED | Posted: 22 February 2021 doi:10.20944/preprints202102.0495.v1

1. Introduction

The developing crisis of environmental contamination is a decisive imperative for the green chemistry community sustainable growth, leading to energy depletion [1, 2]. Due to anthropogenic contaminants, pharmaceutical effluents are increasingly used by living beings to treat bacterial illnesses [3]. The intrinsic existence of drug chemical compounds has difficulty examining the exhibit suffering even at a low level of chemical concentrations due to inappropriate removal [4]. There were quinolone antibiotics, extensive ofloxacin use, and minimal availability in wastewater systems, the toxic risk to ecosystems, and aquatic systems [5-7]. Thus, the identification and corrections of these environmental pollutants are more important, and it is a matter of concern to the scientific community for developing new techniques and doing further research to eradicating the burning problems. Due to their widespread use, quinolones and their metabolites are mostly discharged and gathered in aquatic environments [8]. For example, a common 3rd generation fluoroquinolone antibiotic ofloxacin is detected in municipal sewage up to 31.7μg/L [9]. The numerous antibiotics wastes are then charged to various aquatic environment ecosystems, drinking water, and underground water. The level of antibiotic concentrations is relatively low in aquatic environments, except for waste effluent from the polluting pharmaceutical industry and hospitals [10-13].

Although somewhat efficient, traditional water purification methods such as biodegradation and chlorination cannot efficiently eliminate ofloxacin [14], and induce more toxic byproducts [15-16]. Therefore, it is still essential to improve effective and environmentally eco-friendly strategies to remove ofloxacin from wastewater and other aquatic environments. Photocatalyst analysis has proven to be a promising candidate for the degradation of ofloxacin due to its highly efficient method of removal of biologically resistant antibiotics. To efficiently use the visible light source, it is suitable for the ternary catalyst of visible light active photocatalysts [17-20]. TiO_2 nanoparticles are widely used to decompose harmful chemicals such as phenolic, drug molecules, and dye molecules [21]. Its low functionality in a visible light source for the research society to divide strategies improves such TiO_2 catalysts stimulant's performance, binding to other oxides [22-24]. A number of hybrid composite semiconducting materials has been analyzed to reduce photo electron-hole recombination to improve the large spectral active to wider wavelength such as $BiVO_4$-TiO_2 [25], TiO_2/SiO_2 [26], CdS/TiO_2 [27], ZnO/TiO_2 [28], $TiO_2/SiO_2/Bi_2O_3$ [29], CeO_2/ZnO [30], WO_3/TiO_2 [31], and SnO_2/ZnO [32]. In such a system lead to a possible gradient

Preprints (www.preprints.org) | NOT PEER-REVIEWED | Posted: 22 February 2021 doi:10.20944/preprints202102.0495.v1

in the interface. This suppresses the recombination of the charge carriers and expands the spectral active to a wider wavelength. Connecting TiO_2 to a short-band structure material is capable of enhancing solar consumption at the same time reducing recombination of electrons and holes created by photo-generation. In this short-band structure semiconductor material, bismuth molybdate has effective and suitable material of researchers attribute the best action to the visible source and control ability structural morphology in accordance alternative layer of $[Bi_2O_2]^{2+}$ and MoO_4^{2-} [33-36].

More research was organized to develop a highly capable Bi_2MoO_6/TiO_2 hybrid structure but still had its photodegradation efficiency underwent low visible source rarely anxious. Under weak visible light illumination, are low carriers created by photo-generation during photoreduction process than that of strong-light radiation, and therefore efficient absorption and use of visible light radiation are very important in photocatalysis. It is well known that active photogeneration, separation, and photo-generated electron holes play a significant role in photocatalytic degradation, which can be controlled by material composition and microstructure. Therefore, it is needed to purpose a good catalyst, Bi_2MoO_6-rGO-TiO_2, to enhance the absorption of light towards photodegradation [37-39]. From the point of view of the catalyst constitution of Bi_2MoO_6/TiO_2 compound, the bare Bi_2MoO_6 catalyst can actively absorb visible sources, so it needs to extend the active optically active of TiO_2 to the visible region to enhance the production of the carriers generated by the photogeneration [40]. Moreover, these two catalytic materials can make heterojunction, thus improve the separation of the carriers generated by the photogeneration. On the other hand, specialized structures significant function in the degradation performance of photocatalyst [41].

In recent years, reduced graphene oxide-based photocatalyst has excellent and much attention for its ability to solve environmental contamination problems. Reduced Graphene oxide is a two-dimensional honeycomb structural material that is a perfect receptor and transporter for more electron transport, large surface area, and photo-generated electrons [42, 43]. Many researchers have recommended that the graphene-based hybrid semiconductor improve photocatalytic performance based on the absorption of higher contamination and reduce the level of photo-generated electron-hole recombination, increase electron mobility, and enhance the absorbance light range [44]. Further, to improve the properties, noble metal nanoparticles have been introduced, which significantly enhance the photoreduction efficiency of graphene-TiO_2 and

Preprints (www.preprints.org) | NOT PEER-REVIEWED | Posted: 22 February 2021 doi:10.20944/preprints202102.0495.v1

improve the visible region light absorption capacity [45]. This noble metal/alloy can prevent electron-hole pairs from recombination.

The present research demonstrates that the ternary composite Bi_2MoO_6-rGO-TiO_2 material was synthesized using hydrothermal method. Further, the introduction of Bi_2MoO_6-rGO-TiO_2 has been to improve the photocatalytic degradation efficiency of ofloxacin under visible light illumination, and the possible photocatalytic mechanism has been deduced.

2. Experimental section

$Ti(C_4H_9O)_4$, $Bi(NO_3)_3.6H_2O$, $Na_2MoO_4.2H_2O$, Graphite, HCl and $KMnO_4$, and H_2O_2 were purchased from Daejung Co., Korea.

2.1. Synthesis TiO_2

Firstly, 2 mL of Tetrabutyl titanate were added slowly into concentrated HCl with strong magnetic starrier. The above-mixed solution was diluted using deionized water to adjust the volume of 75 mL. Then, the solution was stirred for 2 h, and the total solution were shifted into a 100 mL Teflon-lined autoclave and closed. The simple hydrothermal preparation was performed at 150 °C for 5 h underwent oven. After the autoclave was cooled under atmospheric condition, the yield was obtained and isolated by centrifuged, repeatedly cleaned with double distilled water, and finally heated at 110 °C underwent a vacuum oven.

2.2. Synthesis of Bi_2MoO_6-TiO_2

The Bi_2MoO_6-TiO_2 was synthesized by mixing 1.3 mmol of $Bi(NO_3)_3.5H_2O$ and 0.65 mmol of $Na_2MoO_4.2H_2O$ with 5 mL of ethylene glycol. Then, the 40 mL ethanol was mixed with stirring for 1 h, and 1 g of TiO_2 nanorods were dispersed into the above solution. After, the autoclave was kept at 160 °C for 24 h. Then, the autoclave was cooling down to atmospheric condition. The sample was cleaned with distilled water, ethanol solution and dried at 80 °C for 12 h in a vacuum oven. Finally, catalysts were heated at 100 °C for 12 h.

2.3. Synthesis of Bi_2MoO_6-rGO-TiO_2

The Graphene oxide (GO) is made up of graphite by Hummer method [45]. The prepared GO (200 mg) were dispersed in 120 mL of distilled water with 0.5 g of urea. The suspension solution was kept at 120 °C for 12 h with the suspension was into 150 mL Teflon lined autoclave. The Bi_2MoO_6-TiO_2 was synthesized by mixing 1.3 mmol of $Bi(NO_3)_3.5H_2O$ and 0.65 mmol of $Na_2MoO_4.2H_2O$ with 5 mL of ethylene glycol. Then, the 40 mL ethanol was mixed with stirring

Preprints (www.preprints.org) | NOT PEER-REVIEWED | Posted: 22 February 2021 doi:10.20944/preprints202102.0495.v1

for 1 h, and 1 g of TiO_2 nanorods and 200 mg of rGO was mixed into the above solution and stirred for 1 h. The above suspension was taken 100 mL stainless autoclave and kept at 180 °C for 24 h. The final suspension was washed several times. The resultant yield was heated at 400 °C for 2 h to obtain Bi_2MoO_6-rGO-TiO_2.With this procedure, appropriate amounts of rGO (1%, 1.5%, 3% and 5%) were used to get Bi_2MoO_6-rGO-TiO_2.

2.4. Photocatalytic measurement

Ofloxacin was used to investigate the photocatalytic degradation efficiency of the Bi_2MoO_6-rGO-TiO_2 ternary catalyst. 40 mg of the ternary photocatalyst was mixed in 100 mL of ofloxacin solution, with a 4×10^{-5} M solution concentration. Then the stirring for 30 min under dark conditions, the solution was shifted to the photoreactor and treated using ABET solar simulator, LS light sources, Korea. The light source intensity was calculated using a digital Lux meter, with an intensity was ~1, 20,000 Lux. 5 mL of the sample was obtained every 15 min interval and centrifuged to get a concentration variation of ofloxacin. A UV-Visible Spectrometer obtained the ofloxacin concentration at its absorption at 288 nm.

X-ray diffractogram for Bi_2MoO_6-rGO-TiO_2 sample was recorded using Pan Alytical Xpert-pro equipped with pw 3050/60 Goniometer in the research laboratory of Rigaku South Korea by operating at 30 kV and 20mA with Cuk_α radiation of λ=1.5405A°. Diffractogram patterns were obtained by continuous scanning from 10.025 to 79.025 of diffraction angle (2θ). JCPDS files were used for peak identification and various crystallinity planes. The morphological, structural analysis (SEM) was obtained using the SEM-HITACHI S-4800 model instrument. HR-TEM was obtained H7600, Hitachi Inc, Japan, and the powder sample was mixed with ethanol, the suspension on the copper grid (400 mesh). XPS elemental analysis was done by Kratos Axis Ultra imaging with Mg anode. Optical bandgap (UV-DRS) was recorded by Neosys-2000 model spectrometer of wavelength range is about 190-1100 nm, Scinco, Korea. The FT-IR functional group investigation of all samples was recorded Nicolet-iS10, Thermo Fisher Scientific, USA, the wavelength range is about 4000-400 cm^{-1}, and used KBr pellet technique. The FT-Raman spectroscopic analysis was done by Horiba-Yvon Lab Ram HR Instrument, the excitation wavelength at λ=633 nm. The photocurrent responsible for the catalyst was recorded by a solar simulator (ABET Technologies), the power density of AM 1.5-100 mW/cm^2. The PL emission

Preprints (www.preprints.org) | NOT PEER-REVIEWED | Posted: 22 February 2021 doi:10.20944/preprints202102.0495.v1

spectra were recorded using FLUORA MAX 4p under the excitation wavelength at 320 nm.

3. Results and discussion

3.1. Powder XRD analysis

Powder XRD is one of the non-destructive analytic techniques for analyzing the crystalline constitution of materials, which is in use since the 1950s. Fig.1 depicted the GO, rGO, Bi_2MoO_6, TiO_2, rGO-Bi_2MoO_6, Bi_2MoO_6-TiO_2, and Bi_2MoO_6-rGO-TiO_2. The PXRD diffraction angle values of 28.31°, 32.56°, 35.93°, 46.66°, 55.46°, and 58.46° are relative to the diffraction pattern of the planes (131), (200), (151), (202), (331), and (262) respectively. The orthorhombic structure of Bi_2MoO_6 is relatively well-matched with the JCPDS file no: 21-0102 and their relative lattice constants a=5.502, b=16.21, c=5.483. No other peaks were observed, which ensure the high purity of the Bi_2MoO_6 [46-47]. The XRD pattern of TiO_2 exhibited the diffraction peak positions at 27.51°, 36.01°, 39.05°, 41.29°, 44.10°, 54.21°, 56.60°, 62.88° and 64.02°, which corresponds to the diffraction planes are (110), (101), (200), (111), (210), (211), (220), (002) and (310) respectively of anatase TiO_2. These results are in good agreement with the JCPDS file no: 21-1276 relative lattice constants a=3.76, b=3.79, c=9.43 [48]. The PXRD patterns of rGO-Bi_2MoO_6 composite material, the diffraction peaks of rGO disappeared in rGO-Bi_2MoO_6 composite material, specifying the disordered restacking of rGO in the rGO-Bi_2MoO_6 composite. There may be attached particles, which prevent restacking, and hence, the diffraction peaks of rGO-layered sheets disappeared. The composite material Bi_2MoO_6-TiO_2 corresponds to the diffraction angles are 27.21°, 27.87°, 31.99°, 35.62°, 40.76°, 46.22°, 53.86°, and 56.26° of their relative planes are (110), (131), (200), (101), (111), (202), (211) and (331) have been observed, the diffracted angles are well-matched with the pure TiO_2 and Bi_2MoO_6. The overall composite material of Bi_2MoO_6-rGO-TiO_2 diffraction angles is well-matched with the pure TiO_2 and Bi_2MoO_6. The diffraction peaks of rGO disappeared in Bi_2MoO_6-rGO-TiO_2 composite material due to disordered restacking of rGO [49]. The diffraction peak at 10.59 corresponds to the planes (001) relative to the facet of Graphene Oxide, and the planes of (002) correspond to the rGO. This result suggests that the XRD pattern of pure graphite and the corresponding planes of (002) indicated the graphitic nature.

Preprints (www.preprints.org) | NOT PEER-REVIEWED | Posted: 22 February 2021 doi:10.20944/preprints202102.0495.v1

3.2. FE-SEM analysis

The morphology of TiO_2, Bi_2MoO_6, and Bi_2MoO_6-rGO-TiO_2 nanocomposite materials can be identified using FE-SEM images. TiO_2 depicted the rod-like structure and the length of the rod several micrometers (Fig.2a-d). The FE-SEM images of Bi_2MoO_6 reveals that the plate-like structure (Fig.2e-h). Bi_2MoO_6 nanocomposite also depicted a close interaction in composite material, the Bi_2MoO_6-TiO_2 well dispersed on the reduced graphene oxide sheets, which may improve the photocatalytic performance. Moreover, Bi_2MoO_6-rGO-TiO_2 ternary composite, Bi_2MoO_6 nanoparticles on the rGO nanosheets surface, and TiO_2 rods can be observed in ternary composite material (Fig.2i-l). Reduced graphene oxide depicted that the sheet-like structure and intercalation of TiO_2 and Bi_2MoO_6 on the sheets, demonstrate that graphite powder is exfoliated into few-layered reduced graphene oxide is obtained.

To investigate the structural morphology and mapping analysis was performed. The results are depicted in the fig.3a-d. Fig.3a-d showed the HR-TEM images of the Bi_2MoO_6-rGO-TiO_2 with various magnification, exhibited that the Bi_2MoO_6 and TiO_2 rods were well dispersed on the surface of reduced graphene oxide and the intercalation between the rGO sheets. From Fig.3e-h, the transparent rGO sheets with TiO_2 rods and Bi_2MoO_6 particles are well interfaces in composite materials. The enlarged two-spots of the HR-TEM images with the lattice fringes at 3.12 and 3.13 Å among the (101) and (101) lattice crystalline planes relative to TiO_2 rod (Fig.4. a-c). Another enlarged two-spots of the HR-TEM images depicted that the lattice fringes are 3.15 and 3.15 Å among the (131) and (131) crystalline lattice planes, which relative to the Bi_2MoO_6 particles (Fig.4. d-f). The lattice planes were identified using Gatan microscopy suite software inbuilt with HR-TEM (insert 4b). The elemental mapping and EDX analysis exhibited the elemental compositions and identified the presence of Bi, Mo, Ti, C, and O, respectively (Fig.5. a-f).

3.3. XPS chemical composition:

XPS investigation can provide more elemental constitutions and chemical states of the Bi_2MoO_6-rGO-TiO_2 compound. The presence of all chemical components was investigated from survey XPS spectra Fig.6a. Furthermore, the Bi 4f XPS spectrum of the Bi 4f level has two intense peaks observed at 158.9 eV and 164 eV, which can be assigned as Bi $4f_{7/2}$, and Bi $4f_{5/2}$, and the peak at 160.3 and 165.7 eV are attributed to the Bi $4f_{7/2}$ and Bi $4f_{5/2}$ (Fig.6b). The observed binding energy values are perfect matched with the oxidation of Bi^{+3}. Furthermore, the Mo 3d level

Preprints (www.preprints.org) | NOT PEER-REVIEWED | Posted: 22 February 2021 doi:10.20944/preprints202102.0495.v1

depicted strong peak positions at 236.2 eV and 232.9 eV, which can be attributed to the Mo $3d_{3/2}$ and Mo $3d_{5/2,}$ respectively [50] (Fig.6c). Moreover, the binding energy of Mo 3d peak position represents the oxidation state of the Mo^{+6} [51]. The Ti 2p XPS spectrum depicted the two strong peak positions at 458.7, 460.2, and 464.8 eV, relative to the Ti $2p_{3/2}$, Ti $2p_{3/2}$, and Ti $2p_{1/2}$, respectively, which depicted the presence of Ti^{4+} in Bi_2MoO_6-rGO-TiO_2 composite [52] (Fig.6d). The O 1s XPS spectrum has three peak positions at 528.2, 529.8, and 531 eV, respectively (Fig.6e). The peak position at 528.2 eV is assigned to the Mo-O/Bi-O groups, while the peak at 529.8 and 531 eV is similar to that of OH atoms. The C1s spectra have three peaks, one is at 284.8 eV, which is relative to C=C for Sp2 hybrid carbon bonding, and another peak position at 285.8, 288.4 eV is assigned to the C=O carbon atom [53] (Fig.6f). XPS investigation offers recognition for the good attachment of carbon atoms to the surface of the Bi_2MoO_6-TiO_2, finally in the structure of Bi_2MoO_6-rGO-TiO_2 nanocomposites photocatalyst.

3.4. FT-IR spectra analysis

The FT-IR spectra of GO, rGO, Bi_2MoO_6, TiO_2, rGO-Bi_2MoO_6, Bi_2MoO_6-TiO_2, and Bi_2MoO_6-rGO-TiO_2 catalyst are depicted in Fig.7. The FT-IR spectra of GO and rGO described that the high-frequency region attributed to stretching of O-H due to the GO presence of hydroxyl group. The intense peaks are 1232 and 1069 cm^{-1}, which relative to the C-O-C and C-OH stretching, respectively. The band location appeared at 1716 cm^{-1} was assigned to the carboxyl group. The rGO spectra of 1230 cm^{-1} and 1571 cm^{-1} are relative to the C-O and C-C stretching vibration. The high-frequency region O-H groups almost disappeared due to the reduction of GO to rGO [54]. The relative peak positions of Bi_2MoO_6 centered at 3420 cm^{-1} are assigned hydroxyl group in the Bi_2MoO_6, the low-frequency region peaks at 844, 728, and 563 cm^{-1} are assigned to stretching vibration modes of Bi-O and Mo-O groups**,** which is reflected in the structure vibration in the crystal. The peak at 1636 cm^{-1} is relative to the C=C stretching vibration [55]. Two characteristics absorption peak at 728 and 563 cm^{-1} are close with symmetric stretching of MoO_6 vibration bonds of the apical oxygen atoms. The broad transmittance peak between 600-400 cm^{-1} relative with the Ti-O-Ti and Ti-O-C in the photocatalyst [56].

3.5. FT-Raman spectral analysis

The FT-Raman spectral analyses of GO, rGO, Bi_2MoO_6-rGO-TiO_2, Bi_2MoO_6-TiO_2, Bi_2MoO_6, rGO-Bi_2MoO_6, rGO-TiO_2, and TiO_2 catalyst are depicted in fig.8. The FT-Raman

Preprints (www.preprints.org) | NOT PEER-REVIEWED | Posted: 22 February 2021 doi:10.20944/preprints202102.0495.v1

spectrum of GO illustrated well-matched with D band peak position at 1353 cm^{-1}, which can be sp3 defects, and the other peak position of G band at 1594 and 1586 cm^{-1}, which can be assigned to the sp2 vibration of carbon atoms, and E_{2g} symmetry of Brillouin zone of phonon modes [57]. Due to the rGO self-healing nature that recovers the hexagonal of carbon atoms, it has also been exhibit that the D band peak remains unchanged when the rGO of the G band peak is reduced from 1594 to 1586 cm^{-1} [58]. This identified to reduced GO into rGO successfully. The 2D band position that is assigned to the graphene property of stacking nature was obtained at 2708 cm^{-1} for rGO. The I_D/I_G ratio was used to determine the structural disorder, which is a small decrement from 0.89 to 0.98 during the reduction of GO into rGO. For this reason, the elimination of an oxide containing groups bonded to the surface of the rGO [59]. The FT-Raman spectra of the rGO-Bi_2MoO_6 catalyst are similar to the Bi_2MoO_6. The peak positions obtained between 600 cm^{-1} to 1000 cm^{-1} were ascribed to Mo-O stretching mode. The band positions at 850 cm^{-1} and 799 cm^{-1} are relative to the A1g of octahedron [60]. The rGO-Bi_2MoO_6 composite material is the introduction of rGO in the composite material. The FT-Raman spectra for TiO_2 and rGO-TiO_2 catalyst depicted the Raman active mode for rutile TiO_2 such as 608, 611 cm^{-1} and 434, 444 cm^{-1} are ascribed To A1g and Eg. The Eg mode is exhibited symmetric stretching vibration of O-Ti-O, and A1g and B1g are ascribed to the anti-symmetric bending vibration of O-Ti-O, respectively [61-62].

3.6. Optical and PL properties

The photocatalytic catalyst efficiency is associated with its capability to absorb light, and the catalyst has a visible region bandgap and enhanced photocatalytic activity. Fig.9 depicted the DRS-UV- visible spectra of the catalyst and the bandgap energy calculated using Taucs plots of the absorption spectra shown in Fig.10. The catalyst absorption range is 408, 421, 470, 479, 450, and 499 nm relative to the TiO_2, rGO-TiO_2, Bi_2MoO_6, rGO-Bi_2MoO_6, Bi_2MoO_6-TiO_2, and Bi_2MoO_6-rGO-TiO_2, respectively. The pure TiO_2 catalyst depicted the absorption region in UV of 408 nm, which is active only UV region, the Bi_2MoO_6, Bi_2MoO_6-TiO_2, rGO-TiO_2, rGO-Bi_2MoO_6, and Bi_2MoO_6-rGO-TiO_2 catalyst, which depicted increased visible region. The photoreduction performance-improved underwent intense visible sources due to the recombination of electrons and holes.

The bandgap energy of bare, binary, and ternary composite was calculated by $[F(R)h\nu]^{1/2}$ using the Kubelka-Munk method [63, 64].

Preprints (www.preprints.org) | NOT PEER-REVIEWED | Posted: 22 February 2021 doi:10.20944/preprints202102.0495.v1

$$F(R)E^{1/2} = \left[\frac{(1-R)^2}{2R} \times h\nu\right]^{1/2}$$

The optical bandgap energies of the TiO_2, rGO-TiO_2, Bi_2MoO_6, rGO-Bi_2MoO_6, Bi_2MoO_6-TiO_2, and Bi_2MoO_6-rGO-TiO_2 corresponds to the 3.00, 2.91, 2.63, 2.55, 2.74, and 2.49 eV, respectively. The optical bandgap of the composite catalyst Bi_2MoO_6-rGO-TiO_2 was a lower bandgap than that of pure and binary catalyst, which improved the photocatalytic activity.

The photoluminescence spectra of photo-generated electron holes in the pure and composite catalyst are shown in fig.11. The PL spectra were measured at an exciting wavelength of 320 nm. The maximum peak intensity is related to photo-induced charge carriers maximum recombination performance, decreasing photocatalytic efficiency. The lower peak intensity corresponds to the lower recombination of electrons and holes, this higher photoreduction efficiency [65]. The PL spectra of the TiO_2, Bi_2MoO_6, Bi_2MoO_6-TiO_2, rGO-TiO_2, rGO-Bi_2MoO_6, and Bi_2MoO_6-rGO-TiO_2. The PL spectra of TiO_2 depicted two peaks at 450 and 466 nm, indicating the surface and irradiative electron-hole recombination of the below conduction band and valance band. Bi_2MoO_6 and rGO-Bi_2MoO_6 represented a PL peak at 466 and 467 nm, the surface cached charge carrier, whose emission energy coincides with the calculated optical bandgap energy. The PL spectra of Bi_2MoO_6-TiO_2 and Bi_2MoO_6-rGO-TiO_2 composite material depicted that the emission peaks at 465 nm and 466 nm, which is ascribed to the photo-generated electron and holes [63]. The emission peak intensity is lower than those of TiO_2, Bi_2MoO_6, Bi_2MoO_6-TiO_2, rGO-TiO_2, rGO-Bi_2MoO_6, which depicted that the Bi_2MoO_6-rGO-TiO_2 lower recombination rate photo-generated electron-holes.

3.7. Photocatalytic degradation of ofloxacin:

The photocatalytic efficiency of bare, TiO_2, rGO-TiO_2, Bi_2MoO_6, rGO-Bi_2MoO_6, Bi_2MoO_6-TiO_2, and Bi_2MoO_6-rGO-TiO_2 composite photocatalyst is depicted in fig.12a. In the dark, during the photocatalytic degradation process in the absence of photocatalyst, there are no major changes in ofloxacin concentration obtained over time. The ofloxacin was stable under visible light illumination. The maximum decomposition of 92.3% using Bi_2MoO_6-rGO-TiO_2 in 120 min underwent visible light irradiation. With TiO_2, rGO-TiO_2, Bi_2MoO_6, rGO-Bi_2MoO_6, Bi_2MoO_6-TiO_2, and Bi_2MoO_6-rGO-TiO_2, the decomposition efficiency percentages are 21.3%, 28.3%, 41.2% 67.2%, and 92.3% in 120 min. The maximum performance of Bi_2MoO_6-rGO-TiO_2

Preprints (www.preprints.org) | NOT PEER-REVIEWED | Posted: 22 February 2021 doi:10.20944/preprints202102.0495.v1

composite photocatalyst over other catalysts is due to the synergetic effect of rGO on Bi_2MoO_6-TiO_2 [66].

A series of tests were performed to estimate the optimum photocatalyst load by different photocatalyst weights from 20 to 50 mg (Fig.12b). The decomposition efficiency of various weight ratio of photocatalyst 20, 30, 40 and 50 mg, the removal efficiency are 60.3%, 75.3%, 92.3% and 84.4% respectively. It is noteworthy that the rate percentage of ofloxacin removal gradually increases from 20, 30, and 40 mg with increasing catalyst loading, and then decreases. Furthermore, the load of the photocatalyst is increasing, the adsorbed number of ofloxacin molecules increases. The catalytic removal efficiency is decreases of ofloxacin at maximum catalyst loading at 50 mg is due to the visible light resist by photocatalyst [67]. The higher amount of photocatalyst, which decreases photocatalytic removal efficiency, is due to photons resistance by catalyst particles and rGO sheets in the composite material. The maximum loading of catalyst led to the shading effect, which can reduce the visible light's absorption and strongly resist the photons, causing a decrease of photodecomposition efficiency [68].

The pH is one of the main parameters in the photocatalytic removal process. The effect of pH variation on decomposition performance of ofloxacin was performed from 5 to 9. From Fig.12c, increasing in pH level from 5 to 9, the photocatalytic removal performance is gradually increased from 67.7%, 92.3%, and 81.1% respectively, suggesting the optimum pH value 7 for efficient photocatalytic removal of ofloxacin under visible light irradiation. The point of zero charges (PZC) for TiO_2 was calculated to be 6.5 and pH level less than that of PZC, the photocatalyst surface is positive charged, and pH value is greater than PZC, it is negative charged [69, 70]. The optimization of rGO in the ternary composite catalyst was analysed with different rGO percentages are 1%, 1.5%, 3% and 5% in composite material to use for the decomposition of ofloxacin, which relative to the decomposition rate were 73%, 80.7%, 92% and 88% respectively (Fig.12d). The increases of rGO content, the photocatalytic decomposition was increased up to 3% of rGO, then decreased decomposition performance with 5% of rGO, this due to the blocking of photons entering the solution by rGO sheets on the surface of the catalyst. The 5% of rGO is incited to the shading effect, which can reduce the light absorption by rGO, reduce the degradation efficiency [71]. The UV absorbance spectra depicted that the increasing time, and the decreasing UV absorbance intensity, which shows the degradation of ofloxacin (Fig.13.).

Preprints (www.preprints.org) | NOT PEER-REVIEWED | Posted: 22 February 2021 doi:10.20944/preprints202102.0495.v1

The linear plot Ln(C/C_0) Vs ofloxacin removal time was shown in the fig.14a-d. In the pseudo-first-order kinetics model, ofloxacin degradation was decreased with increasing time. The first-order kinetics linearity constant values for decomposition of ofloxacin using various catalyst TiO_2, rGO-TiO_2, Bi_2MoO_6, rGO-Bi_2MoO_6, Bi_2MoO_6-TiO_2, and Bi_2MoO_6-rGO-TiO_2 are calculated to be 0.0017, 0.0024, 0.0041, 0.0055, 0.0090, and 0.0174 min^{-1} respectively. The ofloxacin decomposition obeyed the pseudo-first-order kinetics linearity model with the decomposition rate constant values at 0.0174 min^{-1}, which was more efficient than that of pure and binary catalyst. Figure 2 depicted that the pseudo-first-order kinetics curves for the different ternary catalyst dosages of 20 to 50 mg are 0.0077, 0.0111, 0.0177, and 0.0150 min^{-1}, respectively. The efficient decomposition of catalyst is 40 mg, which is the optimum level of catalyst for the degradation of ofloxacin with Bi_2MoO_6-rGO-TiO_2. The kinetics rate constant for different pH values are pH 5, 6, and 7 relatives to the 0.0092, 0.0177 and 0.0138 min^{-1} respectively, the pH 7 is achieved maximum rate constant at 0.0177 min^{-1} is to be optimized level. The kinetics rate constant for different rGO content are 1%, 1.5%, 3% and 5% in composite material, which relative to the rate constant are 0.0108, 0.0135, 0.0191 and 0.0168 min^{-1} respectively. The optimum level is 3% of rGO in ternary composite material.

3.8. Photodecomposition enhancement mechanism

The photocurrent transient density of all photoelectrodes with the switch on and off visible light illumination as depicted in Fig.15a. The photocurrent density of the Bi_2MoO_6-rGO-TiO_2 photoelectrodes higher than the others and the illumination of the Bi_2MoO_6-rGO-TiO_2 photoelectrode has a suitable Bi_2MoO_6 level by managing the time of reaction. The optical photocurrent density of Bi_2MoO_6-rGO-TiO_2 refers to the most extensive photo-generated electrons [72]. Excellent photocurrent transformation means that the synthesized photoelectrode has an efficient visible light active, macropian carrier lifespan, and a less recombination rate. The photoelectrode interface resistance illustrates photo-induced separation and charge carrier transmission performance [73, 74]. A possible photodegradation mechanism was presented. This is because the conduction band and valance band levels of Bi_2MoO_6 and TiO_2 are negative, therefore can form at the type-II heterojunction interface of Bi_2MoO_6-rGO-TiO_2. As depicted in Scheme 1, the catalyst can absorb many photons underwent visible region by the combined absorption of Bi_2MoO_6-rGO-TiO_2. The electrons in the VB of the photocatalyst are stimulated through the photon energy and go to the CB. In the type-II heterojunction, the electrons in Bi_2MoO_6

Preprints (www.preprints.org) | NOT PEER-REVIEWED | Posted: 22 February 2021 doi:10.20944/preprints202102.0495.v1

CB are transferred to TiO_2, and the holes in TiO_2 of VB are converted to Bi_2MoO_6 of VB with the help of an internal semiconducting electric field. To identification of electron migration among the Bi_2MoO_6 and TiO_2 catalyst was studied by XPS spectra (fig.15b,c). The valance band edge positions are calculated from VB XPS spectra of the Bi_2MoO_6 and TiO_2, relative to valance band potential 2.33 eV and 2.95 eV, respectively. The concentrated electron has enough power to reduce the surface of oxygen molecules [75], but concentrated holes have a weaker ability to oxidize OH. The O_2 plays a significant role in the decomposition of ofloxacin. Type-II heterojunction formation effectively prevents and promote the electron and hole recombination, with photocatalyst surface O_2/OH to form active groups.

Reduced graphene oxide has more surface area, and it is a two dimensional integrated large bonding structure. It is highly absorptive and capable of absorbing large numbers of ofloxacin molecules on its surface are composed of π-π [76]. Due to its low resistance, electron migration, recombination of photocatalytic electron and hole are suppressed. Photo-generated electron and holes are separated, thus prolonging the life of the photo-generated electron and offering the most active free radicals to charge and contribute in photocatalytic decomposition of ofloxacin. Therefore, Bi_2MoO_6-rGO-TiO_2 revealed more photocatalytic degradation than Bi_2MoO_6, TiO_2, and, besides, improved the visible-light catalysis function of Bi_2MoO_6-rGO-TiO_2.

3.9. Detection of reactive species:

To recognize the photocatalytic removal mechanism of Bi_2MoO_6-rGO-TiO_2 composite catalyst with ofloxacin. Triethanolamine (TEOA-1 mmol in100 mL) was used as a scavenger of the hole (h^+), benzoquinone (BQ-0.1 mmol in 100 mL) for $O_2^{\bullet-}$ and isopropyl alcohol (IPA-0.1 mmol in 100 mL) for $^{\bullet}OH$ scavenger were used to identify the oxidative species. Fig.15d suggested that the decomposition performance of ofloxacin was diminished after adding BQ. Nevertheless, the photocatalytic removal performance was reduced in the presence of IPA and TEOA under visible light. In, especially with BQ, the photocatalytic removal of ofloxacin is often slower than that of IPA. The significant role of superoxide radicals ($O_2^{\bullet-}$) in the photocatalytic removal of ofloxacin under visible light illumination.

The ternary photocatalyst photocatalytic material stability and reusability are essential for the real application part. The successive cycle runs of ofloxacin with the Bi_2MoO_6-rGO-TiO_2 catalyst under visible light illumination were performed to assess its cycle stability. Every cycle runs recovered the catalyst by centrifugation and then cleaned with deionized and dried at 60 °C

Preprints (www.preprints.org) | NOT PEER-REVIEWED | Posted: 22 February 2021 doi:10.20944/preprints202102.0495.v1

for overnight. The obtained photocatalyst was utilized for the next catalyst runs, as depicted in the cycle test (Fig.16a). The photocatalytic decomposition efficiency was reduced slightly decreased in the fifth cycle run. In this decrement, effectiveness is attributed to the dissolution of catalyst and photo corrosion of the catalyst. Furthermore, the XRD diffraction pattern of Bi_2MoO_6-rGO-TiO_2 ternary catalyst was investigated before the reaction and after five consecutive runs of catalyst (fig.16b). This depicted that the XRD diffraction intensity of peak position was decreased slightly from initial decomposition. Hence, the above test results confirm that the photocatalyst has high stability.

To show the advantages of Bi_2MoO_6-rGO-TiO_2 ternary photocatalyst were compared with previous literature for ofloxacin decomposition, selected previous review results have been related in table 1. This current work is related to the literature review, according to the photocatalyst, ofloxacin, source of light, pH, catalyst dosage, degradation time, and degradation percentage [77-84]. The photocatalyst such as Bi_2MoO_6, ZnO/Bi_2MoO_6, Zeolite-Boron-TiO_2, BiOCl/BiOBr-$Bi_{24}O_{31}Br_{10}$, $Sm_2Ti_2O_7$/1HZSM-5, CdS/TiO_2, Bi_2MoO_6, and ZnO/CdS has been utilized for the degradation of ofloxacin. They need a longer time for degradation. Moreover, Bi_2MoO_6-rGO-TiO_2 is more advantageous than other catalysts.

4. Conclusion

The ternary Bi_2MoO_6-rGO-TiO_2 composite catalyst was prepared by a simple hydrothermal technique. The prepared ternary composite catalyst has increased absorption in the visible region and excellent active visible catalyst than that of bare and binary catalyst for the degradation of emerging pollutant ofloxacin. As the prepared ternary composite catalyst is efficiently decomposition of ofloxacin under visible light illumination within 120 min about 92.3% and it is more effective than that of other catalyst compared with previous literature. Moreover, the ternary photocatalyst depicted low PL and high photocurrent density responsible, exhibited that photon-induced electron-hole recombination was suppressed and charge separation is effective. The rGO is an excellent electron transfer performance and enhanced the stability of the photocatalytic reaction. The perfect cycling stability of the Bi_2MoO_6-rGO-TiO_2 was maintained even after five consecutive cycles on photocatalytic degradation reaction performance. The feasible degradation mechanism is proposed for the decomposition of ofloxacin under visible light illumination.

Acknowledgements:

This research was supported by the National Research Foundation of Korea (NRF) grant funded by Korea government MSIT (No.2018R1A2B6004746 and No. 2019R1A5A8080290).

References

[1] R. Asahi, T. Morikawa, T. Ohwaki, K. Aoki, Y. Taga, Visible-Light Photocatalysis in Nitrogen-Doped Titanium Oxides, Science 293 (2001) 269–271.

[2] M. Dahl, Y. Liu, Y. Yin, Composite Titanium Dioxide Nanomaterials, Chem. Rev.114 (2014) 9853–9889.

[3] M.H. Rasoulifard, H. Majidzadeh, F.T. Demneh, E. Babaei, M.H. Rasoulifard, Photocatalytic degradation of tylosin via ultraviolet-activated persulfate in aqueous solution, Int. J. Ind. Chem. 3 (2012) 16.

[4] K.G. Pavithra, P. Senthil Kumar, P. Sundar Rajan, A. Saravanan, M. Naushad, Sources and impacts of pharmaceutical components in wastewater and its treatment process: a review, Korean J. Chem. Eng. 34 (2017) 2787–2805.

[5] P. Sukul, M. Spiteller, Fluoroquinolone Antibiotics in the Environment, Reviews of environmental Contamination and Toxicology, Springer New York, New York, NY, (2007) 131–162.

[6] C.C. Lin, H.Y. Lin, L.J. Hsu, Degradation of ofloxacin using UV/H_2O_2 process in a large photoreactor, Sep. Purif. Technol. 168 (2016) 57-61.

[7] Sangeeta Adhikari, Do-Heyoung Kim, Synthesis of Bi_2S_3/Bi_2WO_6 hierarchical microstructures for enhanced visible light driven photocatalytic degradation and photoelectrochemical sensing of ofloxacin, Chem. Eng. J. 354 (2018) 692-705.

[8] A.J. Watkinson, E.J. Murby, S.D. Costanzo, removal of antibiotics in conventional and advanced wastewater treatment: implications for environmental discharge and wastewater recycling, Water Res. 41 (2007) 4164-4176.

[9] J. Radjenovic, M. Petrovic, D. Barcelo, Fate and distribution of pharmaceuticals in wastewater and sewage sludge of the conventional activated sludge (CAS) and advanced membrane bioreactor (MBR) treatment, Water Res. 43 (2009) 831-841.

[10] K. Kümmerer, Antibiotics in the aquatic environment – a review-Part II, Chemosphere, 75 (2009) 435-441.

[11] H.Y. Chen, Y.D. Liu, B. Dong, Biodegradation of tetracycline antibiotics in A/O moving-bed biofilm reactor systems, Bioprocess Biosyst. Eng. 41 (2018) 47–56.

[12] J. Zhao, P. Liu, H. Yuan, Y. Peng, Q. Hong, M. Liu, Rapid detection of tetracycline residues in duck meat using surface-enhanced Raman spectroscopy, J. Spectrosc. 6 (2016) 6.

[13] A. Pena, C.M. Lino, R. Alonso, D. Barceló, Determination of tetracycline antibiotic residues in edible swine tissues by liquid chromatography with spectrofluorimetric detection and confirmation by mass spectrometry, J. Agric. Food Chem. 55 (2007) 4973-4979.

[14] K.D. Brown, J. Kulis, B. Thomson, T.H. Chapman, D.B. Mawhinney, Occurrence of antibiotics in hospital, residential, and dairy effluent, municipal wastewater, and the Rio Grande in New Mexico, Sci. Total Environ. 366 (2006) 772-783.

[15] L. Zhu, B. Santiago-Schubel, H. Xiao, H. Hollert, S. Kueppers, Electrochemical oxidation of fluoroquinolone antibiotics: mechanism, residual antibacterial activity and toxicity change, Water Res. 102 (2016) 52-62.

[16] Z. Zhang, X. Xie, Z. Yu, H. Cheng, Influence of chemical speciation on photochemical transformation of three fluoroquinolones (FQs) in water: kinetics, mechanism, and toxicity of photolysis products, Water Res. 148 (2019) 19-29.

[17] X.J. Wen, C.G. Niu, L. Zhang, C. Liang, H. Guo, G.M. Zeng, Photocatalytic degradation of ciprofloxacin by a novel Z-scheme CeO_2-Ag/AgBr photocatalyst: influencing factors, possible degradation pathways, and mechanism insight, J. Catal. 358 (2018) 141-154.

[18] Y. Hong, C. Li, G. Zhang, Y. Meng, B. Yin, Y. Zhao, W. Shi, Efficient and stable Nb_2O_5 modified g-C_3N_4 photocatalyst for removal of antibiotic pollutant, Chem. Eng. J. 299 (2016) 74-84.

[19] Z. Cai, A.D. Dwivedi, W.N. Lee, X. Zhao, W. Liu, M. Sillanpää, D. Zhao, C.H. Huang, J. Fu, Application of nanotechnologies for removing pharmaceutically active compounds from water: development and future trends, Environ. Sci.: Nano.5 (2018) 27-47.

[20] Q. Chen, L. Chen, J. Qi, Y. Tong, Y. Lv, C. Xu, J. Ni, W. Liu, Photocatalytic degradation of amoxicillin by carbon quantum dots modified $K_2Ti_6O_{13}$ nanotubes: effect of light wavelength, Chin. Chem. Lett. 30 (2019) 1214-1218.

[21] S.K. Kansal, S. Sood, A. Umar, S.K. Mehta, Photocatalytic degradation of Eriochrome Black T dye using well-crystalline anatase TiO_2 nanoparticles, J. Alloys Compd. 581 (2013) 392-397.

[22] T. Ohno, M. Akiyoshi, T. Umebayashi, K. Asai, T. Mitsui, M. Matsumur, Preparation of S-doped TiO_2 photocatalysts and their photocatalytic activities under visible light, Appl. Catal. A 265 (2004) 115-121.

[23] S. Tieng, A. Kanaev, K. Chhor, New homogeneously doped Fe (III)–TiO_2 photocatalyst for gaseous pollutant degradation, Appl. Catal. A 399 (2011) 191-197.

[24] S. Sood, S.K. Mehta, A. Umar, S.K. Kansal, The visible light-driven photocatalytic degradation of Alizarin red S using Bi-doped TiO_2 nanoparticles, New J. Chem. 38 (2014) 3127-3136.

[25] Yan-Ran Lv, Chao-Jun Liu, Run-Kai He, Xin Li, Yue-Hua Xu, $BiVO_4/TiO_2$ heterojunction with enhanced photocatalytic activities and photoelectro chemistry performances under visible light illumination, Mater. Res. Bull.,117 (2019) 35-40.

[26] Qi Jiang, Jian Huang, Baoguo Ma, Zhengcai Yang, Ting Zhang, Xin Wang, Recyclable, hierarchical hollow photocatalyst $TiO_2@SiO_2$ composite microsphere realized by raspberry-like SiO_2, Colloids Surf., A. 602 (2020) 125112.

[27] Y. Hu, D.Z. Li, Y. Zheng, W. Chen, Y.H. He, Y. Shao, X.Z. Fu, G.C. Xiao, $BiVO_4/TiO_2$nanocrystalline heterostructure: a wide spectrum responsive photocatalyst towards the highly efficient decomposition of gaseous benzene, Appl. Catal. B104 (2011) 30-36.

[28] Derya Tekin, Hakan Kiziltas, Hande Ungan, Kinetic evaluation of ZnO/TiO_2 thin film photocatalyst in photocatalytic degradation of Orange G, J. Mol. Liq.,306 (2020) 112905.

[29] C. Ren, W. Qiu, H. Zhang, Z. He, Y. Chen, Degradation of benzene on $TiO_2/SiO_2/Bi_2O_3$ photocatalysts under UV and visible light, J. Mol. Catal. A Chem. 398 (2015) 215-222.

[30] Qian Zhang, Xiaoru Zhao, LibingDuan, Hao Shen, Ruidi Liu, Controlling oxygen vacancies and enhanced visible light photocatalysis of CeO_2/ZnO nanocomposites, J. Photochem. Photobiol. A, 392 (2020) 112156.

[31] Z.F. Huang, J.J. Zou, L. Pan, S. Wang, X. Zhang, L. Wang, Synergetic promotion on photoactivity and stability of $W_{18}O_{49}/TiO_2$, Appl. Catal. B, 147 (2014) 167-174.

[32] R. Lamba, A. Umar, S.K. Mehta, S.K. Kansal, Well-crystalline porous ZnO-SnO_2 nanosheets: an effective visible-light driven photocatalyst and highly sensitive smart sensor material, Talanta, 131 (2015) 490-498.

[33] W. Yu, X. J. Liu, L. K. Pan, J. L. Li, J. Y. Liu, J. Zhang, P. Li, C. Chen and Z. Sun, Appl. Surf. Sci., 319 (2014) 107-112.

[34] A. Yanhui, X. Junling, W. Peifang, W. Chao, H. Jun, Q. Jin and L. Yi, Colloids Surf. A Physicochem. Eng. Asp., 487 (2015).

[35] X. Li, X. Zhou, Q. Gao, J. Yuan, J. Wen, Y. Fang, W. Liu, S. Zhang and Y. Liu, Metal-free carbon nanotube-SiC nanowire heterostructures with enhanced photocatalytic H2 evolution under visible light irradiation, Catal. Sci. Technol., 4 (2015) 2798-2806.

[36] Z.Q. Li, X.T. Chen, Z.L. Xue, Bi_2MoO_6 microstructures: controllable synthesis, growth mechanism, and visible-light-driven photocatalytic activities, Cryst. Eng. Comm., 15 (2013) 498-508.

[37] N. Li, L. Zhu, W. D. Zhang, Y.X. Yu, W.H. Zhang, M.F. Hou, Modification of TiO_2 nanorods by Bi_2MoO_6 nanoparticles for high performance visible-light photocatalysis, 509 (2011) 9770-9775.

[38] Q. Yang, E. Y. Guo, H. Liu and Q. F. Lu, Engineering of Z-scheme 2D/3D architectures with Bi_2MoO_6 on TiO_2 nanosphere for enhanced photocatalytic 4-nitrophenol degradation, J. Taiwan Inst. Chem. Eng., 105 (2019) 65-74.

[39] Z. Y. Liu, Y. D. Song, Q. Y. Wang, Y. Jia, X. Y. Tan, X. X. Du, S. M. Gao, Solvothermal fabrication and construction of highly photoelectrocatalytic TiO_2 NTs/Bi_2MoO_6 heterojunction based on titanium mesh, J. Colloid Interface Sci., 2019, 556, 92-101.

[40] L. Gai, X. Duan, H. Jiang, Q. Mei, G. Zhou, Y. Tian and H. Liu, One-pot synthesis of nitrogen-doped TiO_2nanorods with anatase/brookite structures and enhanced photocatalytic activity, Cryst. Eng. Comm. 14 (2012) 7662-7671.

[41] Y. J. Chen, G. H. Tian, Z. Y. Ren, K. Pan, Y. H. Shi, J. Q. Wang and H. G. Fu, Hierarchical Core–Shell Carbon Nanofiber@$ZnIn_2S_4$ Composites for Enhanced Hydrogen Evolution Performance, ACS Appl. Mater. Interfaces, 6 (2014) 13841-13849.

[42] M. Vanitha, S. Keerthi, N. Vadivel, Balasubramanian, Visible light photocatalysis of Methylene blue by graphene-based ZnO and Ag/AgCl nanocomposites, Desalin. Water Treat. 54 (2015) 2748-2756.

[43] R. Beura, P. Thangadurai, Structural, optical and photocatalytic properties of graphene-ZnO nanocomposites for varied compositions, J. Phys. Chem. Solids. 102 (2017) 168-177.

[44] Y. Ni, W. Wang, W. Huang, C. Lu, Z. Xu, Graphene strongly wrapped TiO_2 for high reactive photocatalyst: A new sight for significant application of graphene, J. Colloid Interface Sci. 428 (2014) 162-169.

[45] X. Zhou, T. Shi, J. Wu, H. Zhou, (001) Facet-exposed anatase-phase TiO_2 nanotube hybrid reduced graphene oxide composite: Synthesis, characterization and application in photocatalytic degradation, Appl. Surf. Sci. 287 (2013) 359-368.

 doi:10.20944/preprints202102.0495.v1

[46] J. Ding, Z. Yang, C. He, X. Tong, Y. Li, X. Niu, H. Zhang UiO-66 (Zr) coupled with Bi_2MoO_6 as photocatalyst for visible-light promoted dye degradation J. Colloid. Interf. Sci., 497 (2017) 126-133.

[47] Y. Tian, F. Zhou, S. Zhan, Z. Zhu, Q. He, Mechanisms on the enhanced sterilization performance of fluorocarbon resin composite coatings modified by g-C_3N_4/Bi_2MoO_6 under the visible-light, J. Photochem. Photobiol. A, 350 (2018) 10-16.

[48] A. Raja, P. Rajasekaran, K. Selvakumar, M. Arivanandhan, S. Asath Bahadur, M. Swaminathan, Efficient Photoreduction of Hexavalent Chromium Using the Reduced Graphene Oxide−Sm_2MoO_6−TiO_2 Catalyst under Visible Light Illumination, ACS Omega, 5 (2020) 6414-6422.

[49] Y. Yang, L.L. Ren, C. Zhang, S. Huang, T.X. Liu, Facile fabrication of functionalized graphene sheets (FGS)/ZnO nanocomposites with photocatalytic property, ACS Appl. Mater. Interfaces, 3 (2011) 2779-2785.

[50] J. Yi, H. Mo, B. Zhang, J. Song, D. Liu, G. Zhuo, CeO_2/Bi_2MoO_6 heterostructured microspheres with synergistic effect for accelerating photo-generated charge separation, Sep. Purif. Technol., 211 (2019) 474-480.

[51] Y. S. Xu, W. D. Zhang, Monodispersed Ag_3PO_4 Nanocrystals Loaded on the Surface of Spherical Bi_2MoO_6 with Enhanced Photocatalytic Performance. Dalton Trans. 42 (2013) 1094-1101.

[52] W. J. Ren, Z. H. Ai, F. L. Jia, L. Z. Zhang, X. X. Fan and Z. G. Zou, Low temperature preparation and visible light photocatalytic activity of mesoporous carbon-doped crystalline TiO_2, Appl. Catal. B. Environ., 69 (2007) 38-144.

[53] Subhajyoti Samanta, Santimoy Khilari, Rajendra Srivastava, Stimulating the Visible-Light Catalytic Activity of Bi_2MoO_6Nanoplates by Embedding Carbon Dots for the Efficient Oxidation, Cascade Reaction, and Photoelectrochemical O_2 Evolution, CS Appl. Nano Mater. 1 (2018) 426–441.

 doi:10.20944/preprints202102.0495.v1

[54] A. Raja, P. Rajasekaran, K. Selvakumar, M. Arunpandian, K. Kaviyarasu, S. Asath Bahadur, M. Swaminathan, Visible active reduced graphene oxide-$BiVO_4$-ZnO ternary photocatalyst for efficient removal of ciprofloxacin, Sep. Purif. Technol., 233 (2020) 115996.

[55] K. Maruthathurai, T. Sivakumar S. Aishwary, Fabrication of sphere-like Bi_2MoO_6/ZnO composite catalyst with strong photocatalytic behavior for the detoxification of harmful organic dyes, Opt. Mater., 109 (2020) 110218.

[56] M.Winter, D.Hamal, X.Yang, H.Kwen, D.Jones, S.Rajagopalan, K. J. Klabunde, Defining Reactivity of Solid Sorbents: What Is the Most Appropriate Metric? Chem. Mater., 21 (2009) 2367-2374.

[57] D.Naumenko, V.Snitka, B.Snopok, S. Arpiainen, H.Lipsanen, Graphene enhanced Raman imaging of TiO_2 nanoparticles. Nanotechnology 23(2012) 465703.

[58] Q.Zheng, Biao Zhang , Xiuyi Lin, Xi Shen, Nariman Yousefi, Zhen-Dong Huang, Zhigang Li, Jang-Kyo Kim, Highly transparent and conducting ultralarge graphene oxide/single-walled carbon nanotube hybrid films produced by Langmuir–Blod get assembly, J. Mater. Chem. 22(2012) 25072.

[59] G.S.H. Thien, A. Pandikumar, N.M. Huang, H.N. Lim, Highly exposed {001} facets of titanium dioxide modified with reduced graphene oxide for dopamine sensing. Sci. Rep. 4(2014) 5044.

[60] Z. Liu, J. Tian, D. Zeng, C. Yu, W. Huang, K. Yang, X. Liu, H. Liu, Binary-phase TiO_2 modified Bi_2MoO_6 crystal for effective removal of antibiotics under visible light illumination, Mater. Res. Bull., 112 (2019) 336-345.

[61] C. Leyva-Porras, A. Toxqui-Teran, O. Vega-Becerra, M. Miki-Yoshida, M. Rojas-Villalobos, M. García-Guaderrama, J.A. Aguilar-Martínez, Low-temperature synthesis and characterization of anatase TiO_2 nanoparticles by an acid assisted sol–gel method, J. Alloys Compd., 647 (2015) 627-636.

[62] J. Yan, G. Wu, N. Guan, L. Li, Z. Li, X. Cao, Understanding the effect of surface/bulk defects on the photocatalytic activity of TiO_2: anatase versus rutile, Phys. Chem. Chem. Phys., 15 (2013)10978-10988.

[63] Zhen Liu, JianT ian, Debing Zeng, Changlin Yu, Weiya Huang, Kai Yang, Xing qiang Liu, Hong Liu, Binary-phase TiO_2 modified Bi_2MoO_6 crystal for effective removal of antibiotics under visible light illumination, Mater. Res. Bull, 12 (2019) 336-345.

[64] Jinliang Lia, Xinjuan, Liu, Zhuo Sun, Likun Pan, Novel Bi_2MoO_6/TiO_2 heterostructure microspheres for degradation of benzene series compound under visible light irradiation, J. Colloid Interface Sci., 463 (2016) 145-153.

[65] Byung Hyun Park, Junhee Lee, Hyerim Park, Jeong Yeon Do, Young soo Kim, Rama Krishna Chava, Misook Kang, Effective charge separation through the sulfur vacancy interfacial in n-CdO/p-CdS bulk heterojunction particle and its solar-induced hydrogen production, J. Ind. Eng. Chem. 91 (2020) 149-166.

[66] A.Raja, P.Rajasekaran, K.Selvakumar, M.Arivanandhan, S.Asath Bahadur, M. Swaminathan, Rational fabrication of needle with spherical shape ternary reduced Graphene Oxide-$HoVO_4$-TiO_2 photocatalyst for degradation of ibuprofen under visible light, Appl. Surf. Sci. 513 (2020) 145803.

[67] K.Selvakumar, A. Raja, M.Arunpandian, K.Stalindurai, P.Rajasekaran, P. Sami, E. R. Nagarajan, M.Swaminathan, Efficient photocatalytic degradation of ciprofloxacin and bisphenol A under visible light using Gd_2WO_6 loaded ZnO/bentonite nanocomposite, Appl. Surf. Sci.481 (2019) 1109-1119.

[68] Y. Li, J. Zhan, L. Huang, H. Xu, H. Li, R. Zhang, S. Wua, Synthesis and photocatalytic activity of a bentonite/g-C_3N_4 composite, RSC Adv. 4 (2014) 11831-11839.

[69] Jung-Chuan Chou, Lan Pin Liao, Study on pH at the point of zero charge of TiO_2 pH ion-sensitive field effect transistor made by the sputtering method, Thin Solid Films, 476 (2005) 57-161.

 doi:10.20944/preprints202102.0495.v1

[70] R. Velmurugan, B. Krishnakumar, B. Subash, M. Swaminathan, Preparation and characterization of carbon nanoparticles loaded TiO_2 and its catalytic activity driven by natural sunlight, Sol. Energy Mater. Sol. Cells, 108 (2013) 205-212.

[71] K. Chang, Z.W. Mei, T. Wang, Q. Kang, S.X. Ouyang, J.H. Ye, MoS_2/graphene cocatalyst for efficient photocatalytic H_2 evolution under visible light irradiation, ACS Nano., 8 (2014)7078–7087.

[72] Y.H. Peng, Q.H. Liu, J.Q. Zhang, Y. Zhang, M.J. Geng, J.Q. Yu, Enhanced visible-light-driven photocatalytic activity by 0D/2D phase heterojunction of quantum dots/nanosheets on bismuth molybdates, J. Phys. Chem. C, 122 (2019) 3738-3747.

[73] J. Zhang, C.L. Shao, X.H. Li, J.Y. Xin, R. Tao, Y.C. Liu, Assembling n-Bi_2MoO_6 nanosheets on electrospun p-$CuAl_2O_4$ hollow nanofibers: enhanced photocatalytic activity based on highly efficient charge separation and transfer, ACS Sustain. Chem. Eng., 6 (2019) 10714-10723.

[74] B.B. Liu, X.J. Liu, M.Y. Ni, C.J. Feng, X. Lei, C. Li, Y.Y. Gong, L.Y. Niu, J.L. Li, L.K. PanSnO_2 as co-catalyst for enhanced visible light photocatalytic activity of Bi_2MoO_6 Appl. Surf. Sci., 453 (2018) 280-287.

[75] L. Wu, F. Li, Y.Y. Xu, J.W. Zhang, D.Q. Zhang, G.S. Li, H.X. Li, Plasmon-induced photo electrocatalytic activity of Au nanoparticles enhanced TiO_2 nanotube arrays electrodes for environmental remediation, Appl. Catal. B-Environ., 164 (2015) 217-224.

[76] J.N. Tiwari, K. Mahesh, N.H. Le, K.C. Kemp, R. Timilsina, R.N. Tiwari, K.S. Kim, Reduced graphene oxide-based hydrogels for the efficient capture of dye pollutants from aqueous solutions, Carbon, 56 (2013) 173-182.

[77] T.Chankhanittha, V.Somaudon, J.Watcharakitti, V.Piyavarakorn, S.Nanan, Performance of solvothermally grown Bi_2MoO_6 photocatalyst toward degradation of organic azo dyes and fluoroquinolone antibiotics, Mater. Lett., 258 (2020) 126764.

 doi:10.20944/preprints202102.0495.v1

[78] T.Chankhanittha, S.Nanan, Visible-light-driven photocatalytic degradation of ofloxacin (OFL) antibiotic and Rhodamine B (RhB) dye by solvo thermally grown ZnO/Bi_2MoO_6 heterojunction, J. Colloid Interface Sci., 582 (2021) 412-427.

[79] H. Li, W. Zhang, Y. Liu, HZSM-5 zeolite supported boron-doped TiO_2 for photocatalytic degradation of ofloxacin, J. Mater. Res. Technol., 9 (2020) 2557-2567.

[80] S. Heidari, M.Haghighi, M. Shabani, Sunlight-activated BiOCl/BiOBr–$Bi_{24}O_{31}Br_{10}$ photocatalyst for the removal of pharmaceutical compounds, J. Clean. Prod, 259 (2020) 120679.

[81] L. Yang, K. Wang, J. Yang, W. Zhang, Role of hydrochloric acid treated HZSM-5 zeolite in $Sm_2Ti_2O_7$/nHZSM-5 composite for photocatalytic degradation of ofloxacin, J. Mater. Res. Technol., 9 (2020) 10585-10596.

[82] A. Kaur, A. Umar, W. A. Anderson, S. K.Kansal, Facile synthesis of CdS/TiO_2 nanocomposite and their catalytic activity for ofloxacin degradation under visible illumination, J. Photochem. Photobiol. A., 360 (2018) 34-43.

[83] G. Gupta, A. Umar, A. Kaur, S.Sood, A.Dhir, S.K.Kansal, Solar light driven photocatalytic degradation of ofloxacin based on ultra-thin bismuth molybdenum oxide nanosheets, Mater. Res. Bull., 99 (2018) 359-366.

[84] T.Senasu, T.Chankhanittha, K.Hemavibool, S.Nanana, Visible-light-responsive photocatalyst based on ZnO/CdS nanocomposite for photodegradation of reactive red azo dye and ofloxacin antibiotic, Mater Sci.Semicond. Process, (2020) 10558.

Preprints (www.preprints.org) | NOT PEER-REVIEWED | Posted: 22 February 2021 doi:10.20944/preprints202102.0495.v1

Figures

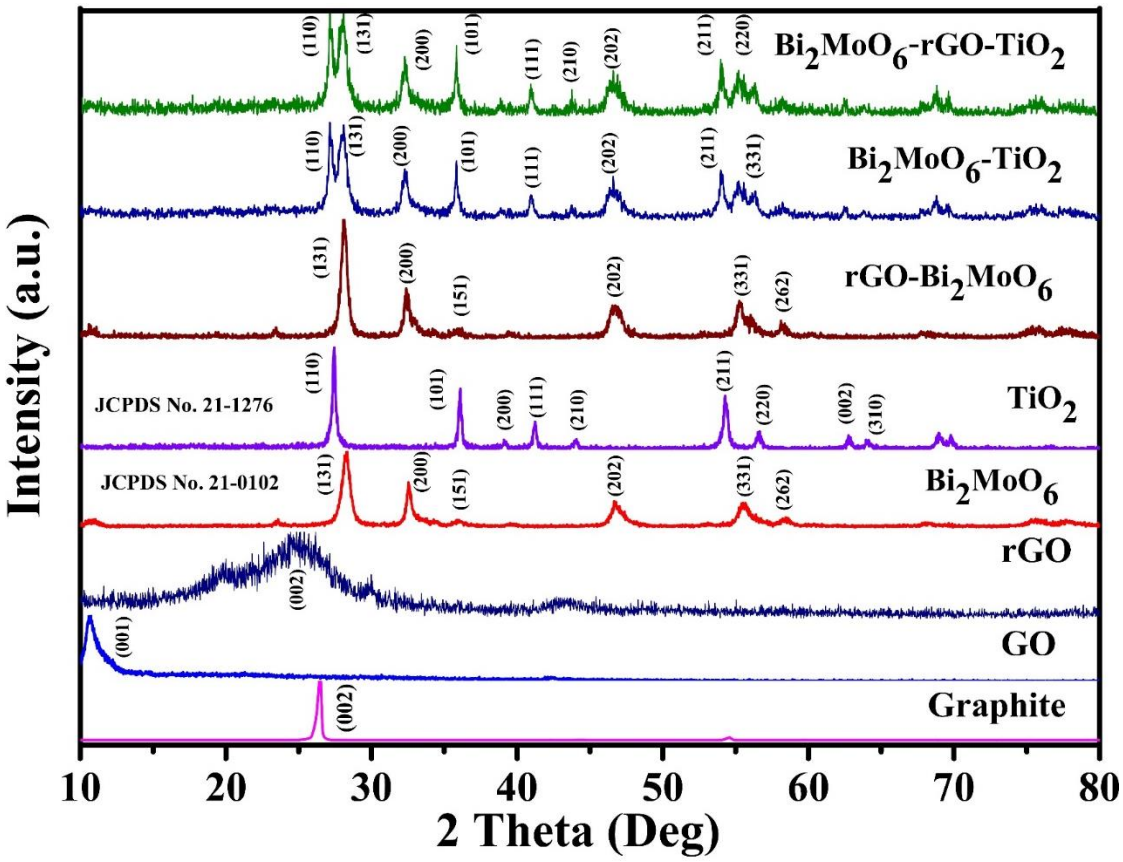

Fig.1. XRD spectra of graphite, GO, rGO, Bi_2MoO_6, TiO_2, rGO-Bi_2MoO_6, TiO_2-Bi_2MoO_6 and Bi_2MoO_6-rGO-TiO_2 nanocomposite

Preprints (www.preprints.org) | NOT PEER-REVIEWED | Posted: 22 February 2021 doi:10.20944/preprints202102.0495.v1

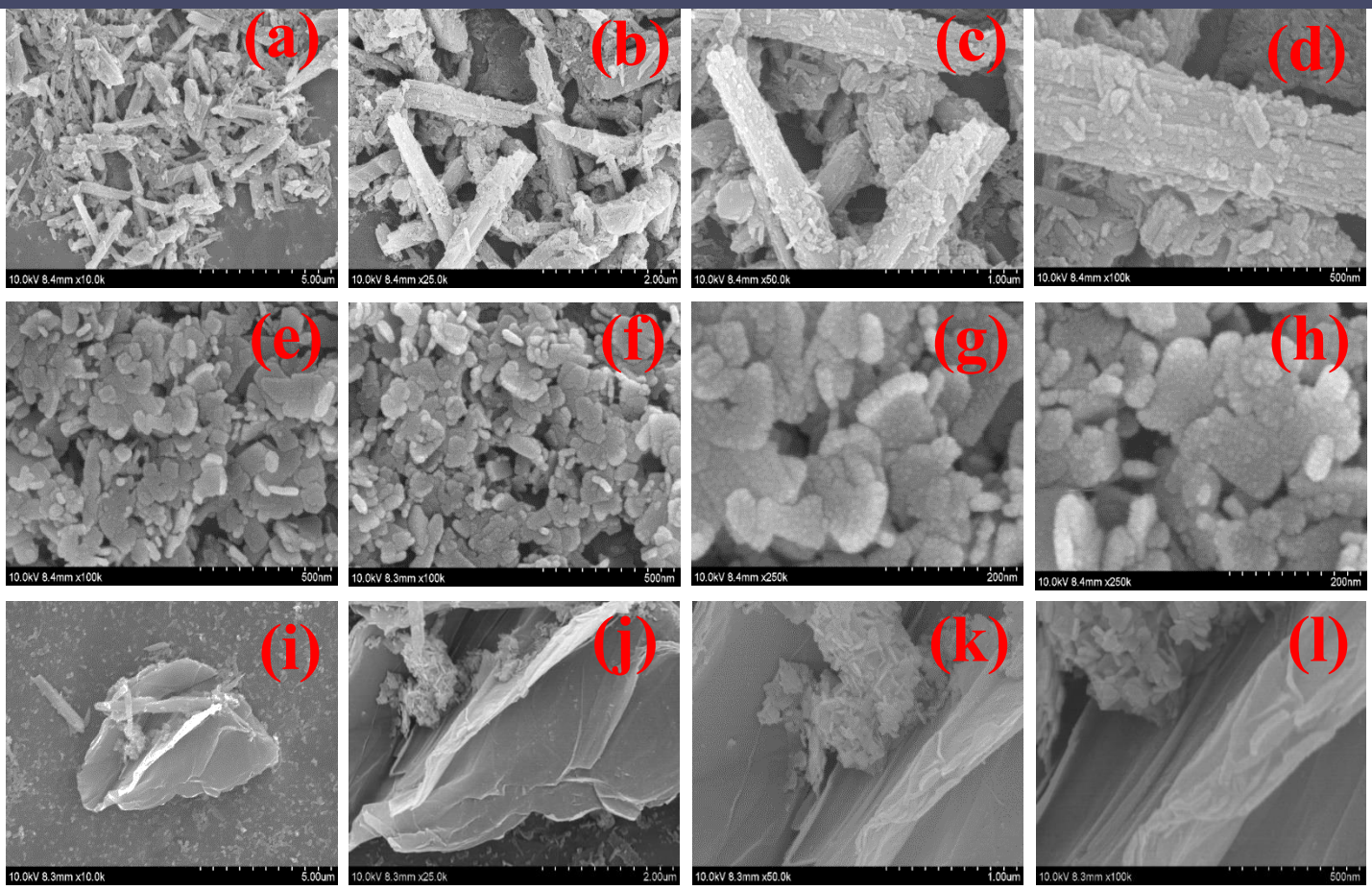

Fig.2. FE-SEM images of TiO_2 (a-d), Bi_2MoO_6 (e-h), and (i-l) Bi_2MoO_6-rGO-TiO_2 nanocomposite

Preprints (www.preprints.org) | NOT PEER-REVIEWED | Posted: 22 February 2021 doi:10.20944/preprints202102.0495.v1

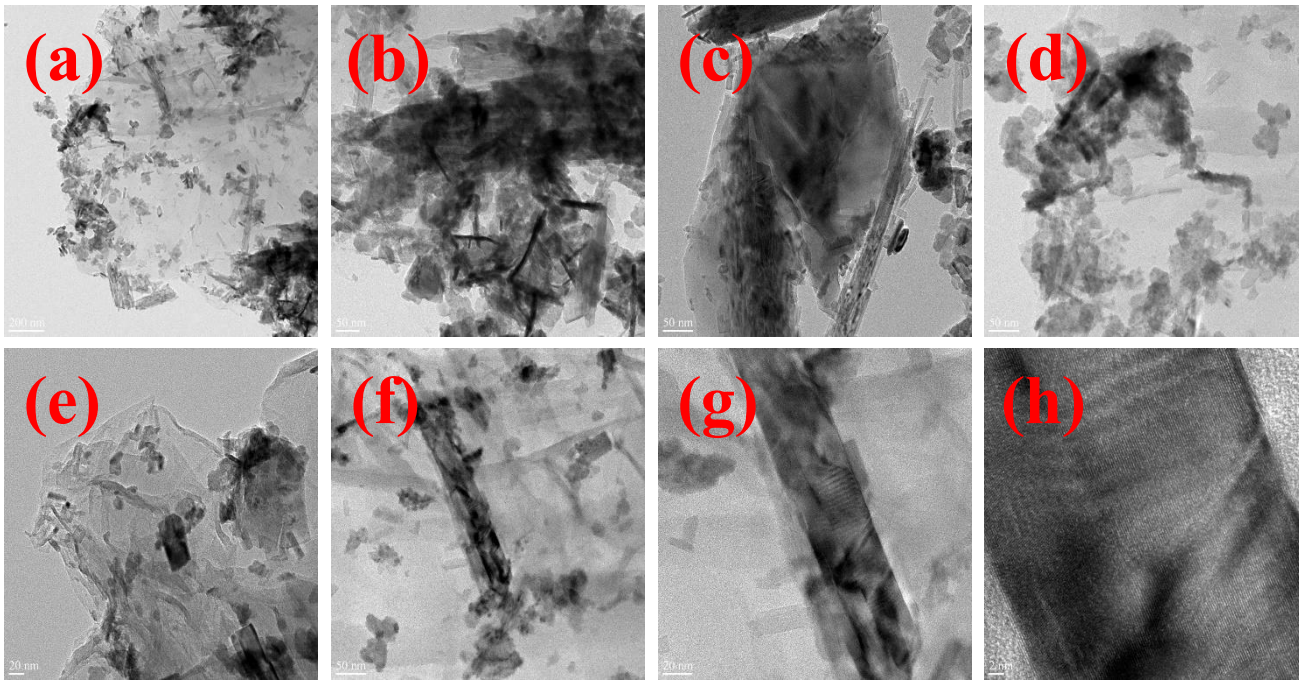

Fig.3. TEM images of Bi_2MoO_6-rGO-TiO_2 nanocomposite

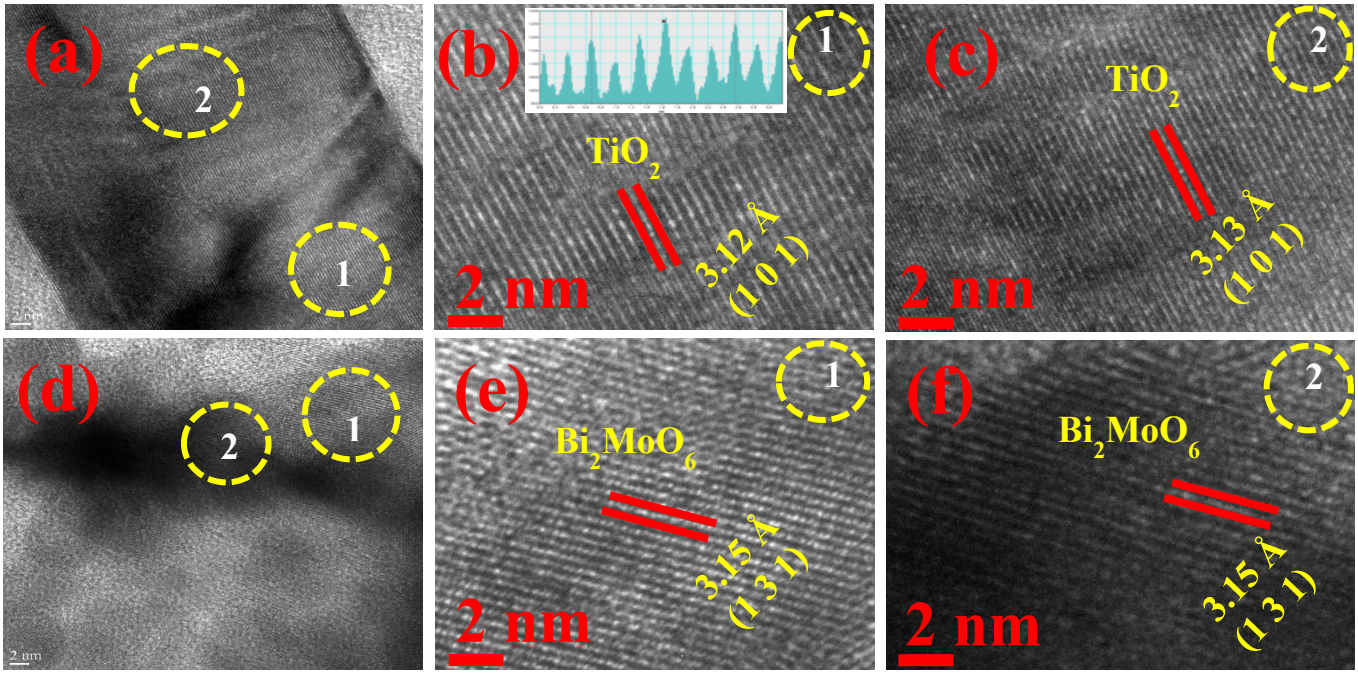

Fig. 4. HR-TEM Images of Bi_2MoO_6-rGO-TiO_2 (a-f)

Preprints (www.preprints.org) | NOT PEER-REVIEWED | Posted: 22 February 2021 doi:10.20944/preprints202102.0495.v1

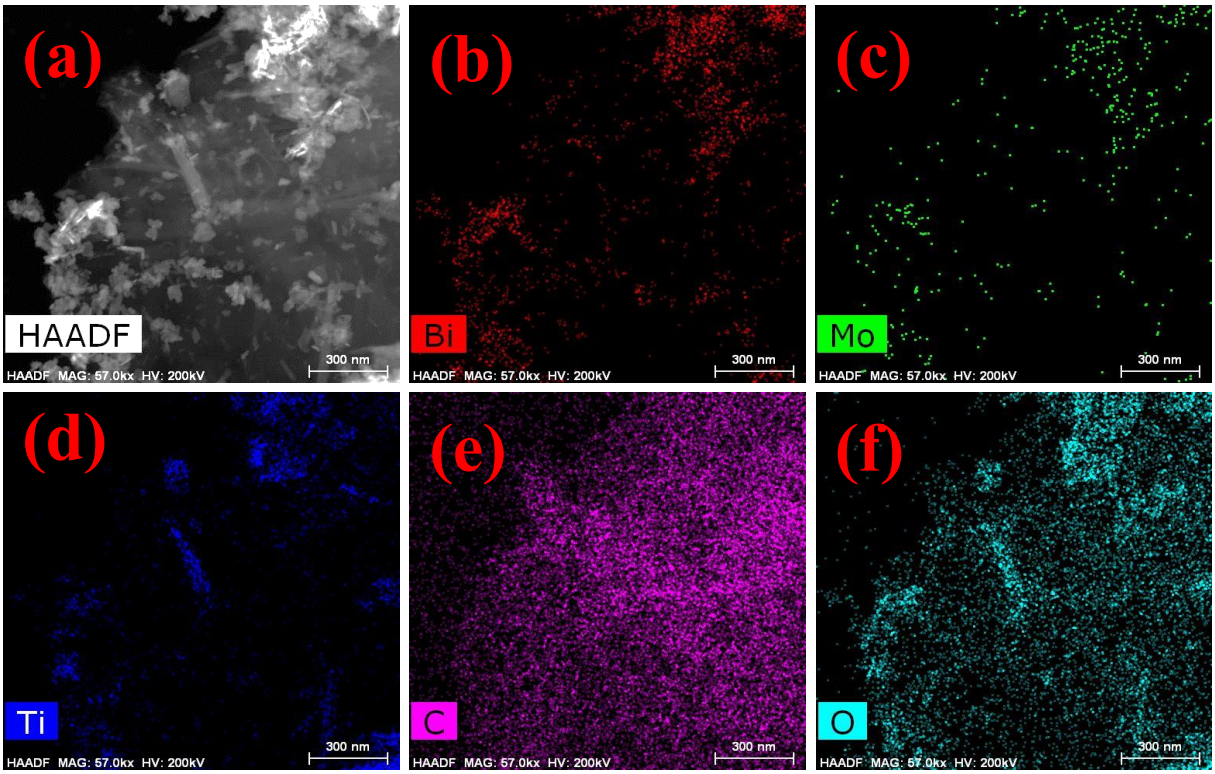

Fig.5. Elemental mapping spectra of Bi_2MoO_6-rGO-TiO_2 nanocomposite

Preprints (www.preprints.org) | NOT PEER-REVIEWED | Posted: 22 February 2021 doi:10.20944/preprints202102.0495.v1

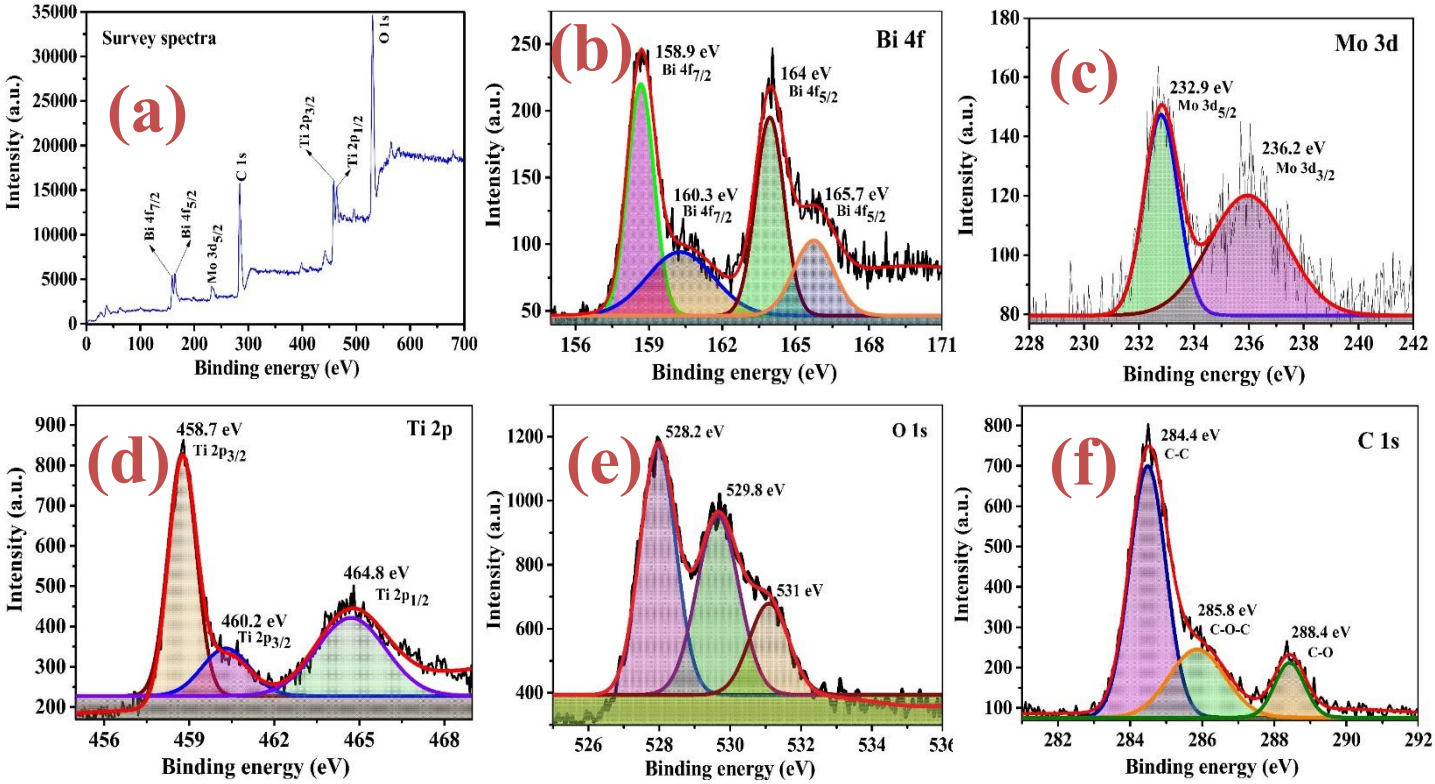

Fig.6. XPS spectrum of the Bi_2MoO_6-rGO-TiO_2 nanocomposite, survey spectrum (a), Bi 4f spectrum (b), Mo 3d spectrum (c), Ti 2p spectrum (d), C 1s spectrum (e), and O 1s spectrum (f)

Preprints (www.preprints.org) | NOT PEER-REVIEWED | Posted: 22 February 2021 doi:10.20944/preprints202102.0495.v1

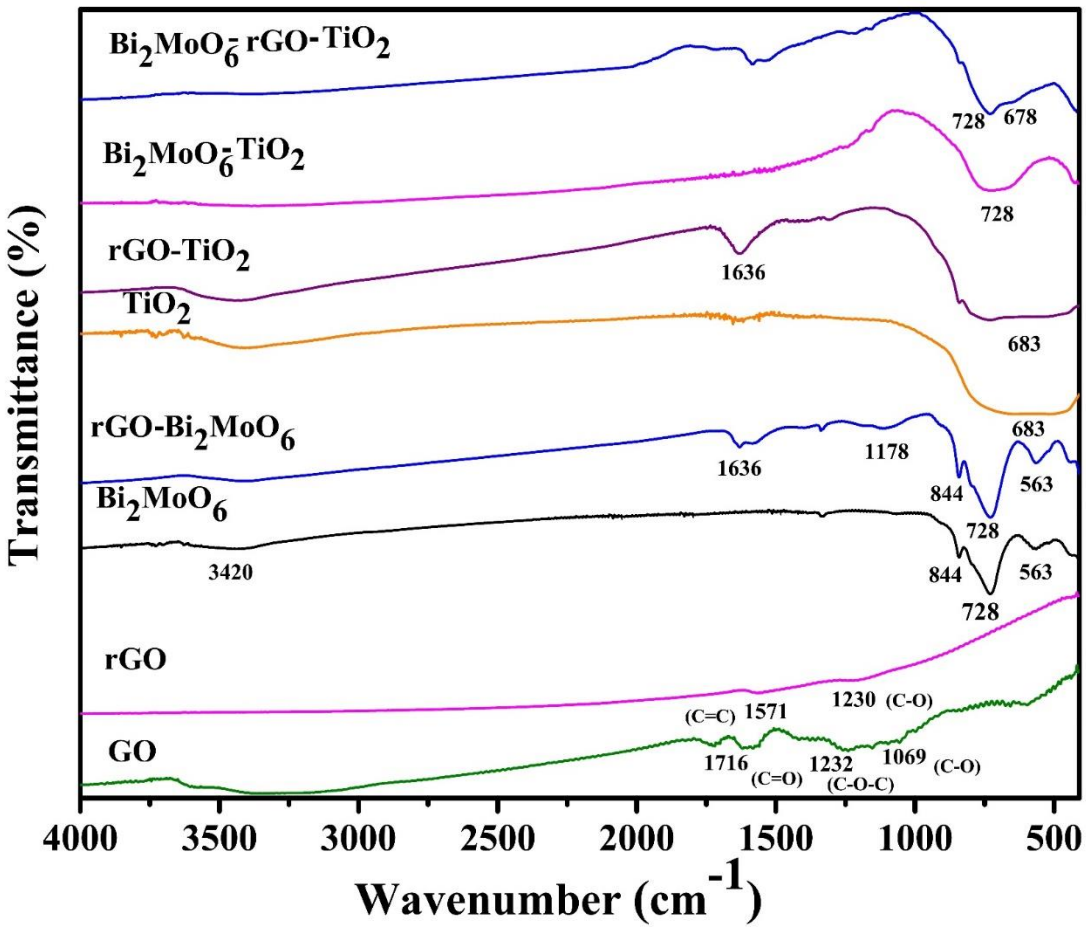

Fig.7. FT-IR spectra of GO, rGO, Bi_2MoO_6, rGO-Bi_2MoO_6, TiO_2, rGO-TiO_2, Bi_2MoO_6-TiO_2 and Bi_2MoO_6-rGO-TiO_2 nanocomposite

Preprints (www.preprints.org) | NOT PEER-REVIEWED | Posted: 22 February 2021 doi:10.20944/preprints202102.0495.v1

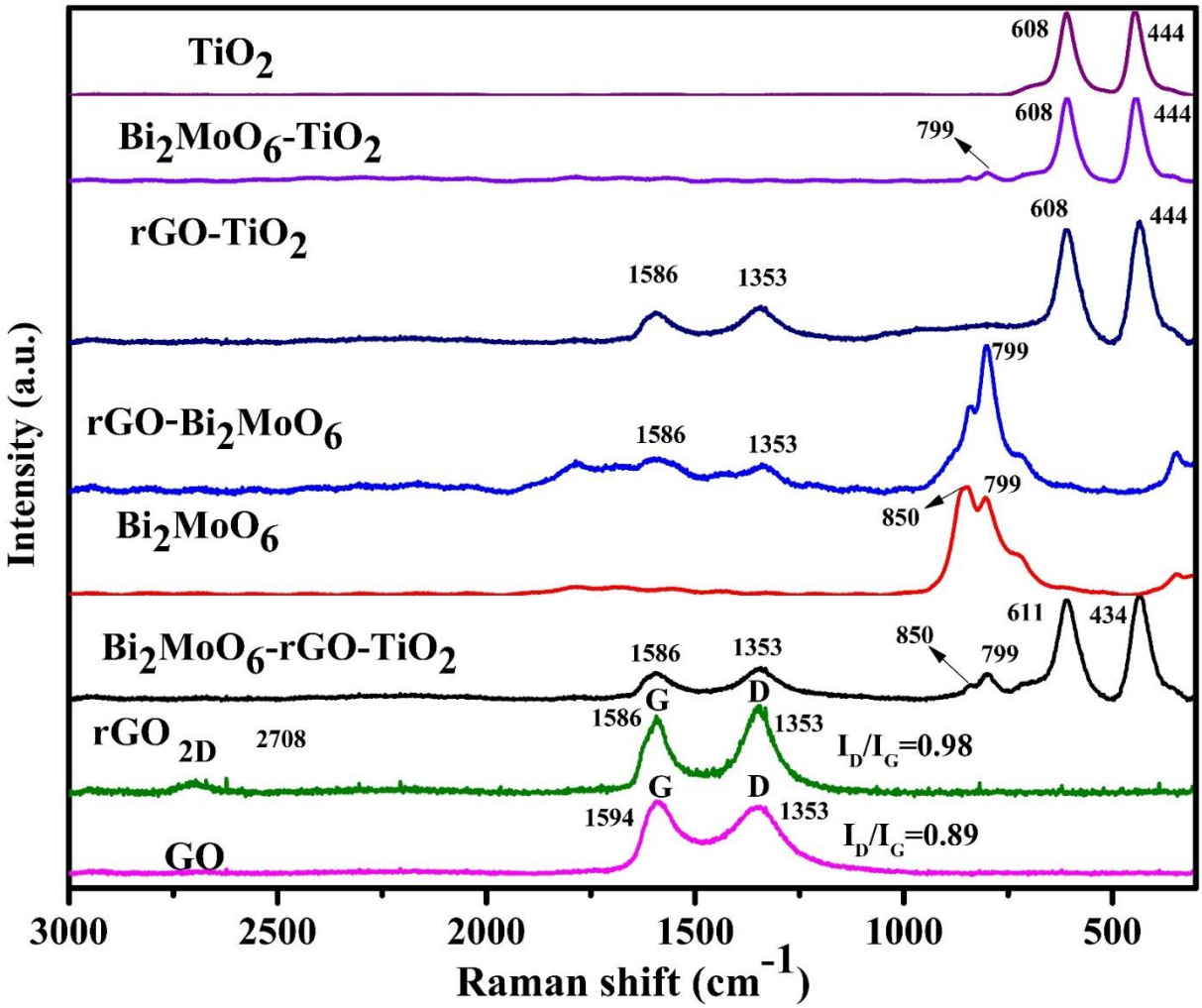

Fig.8. FT-Raman spectra of GO, rGO, Bi_2MoO_6-rGO-TiO_2, Bi_2MoO_6, rGO-Bi_2MoO_6, rGO-TiO_2, Bi_2MoO_6-TiO_2 and TiO_2

Preprints (www.preprints.org) | NOT PEER-REVIEWED | Posted: 22 February 2021 doi:10.20944/preprints202102.0495.v1

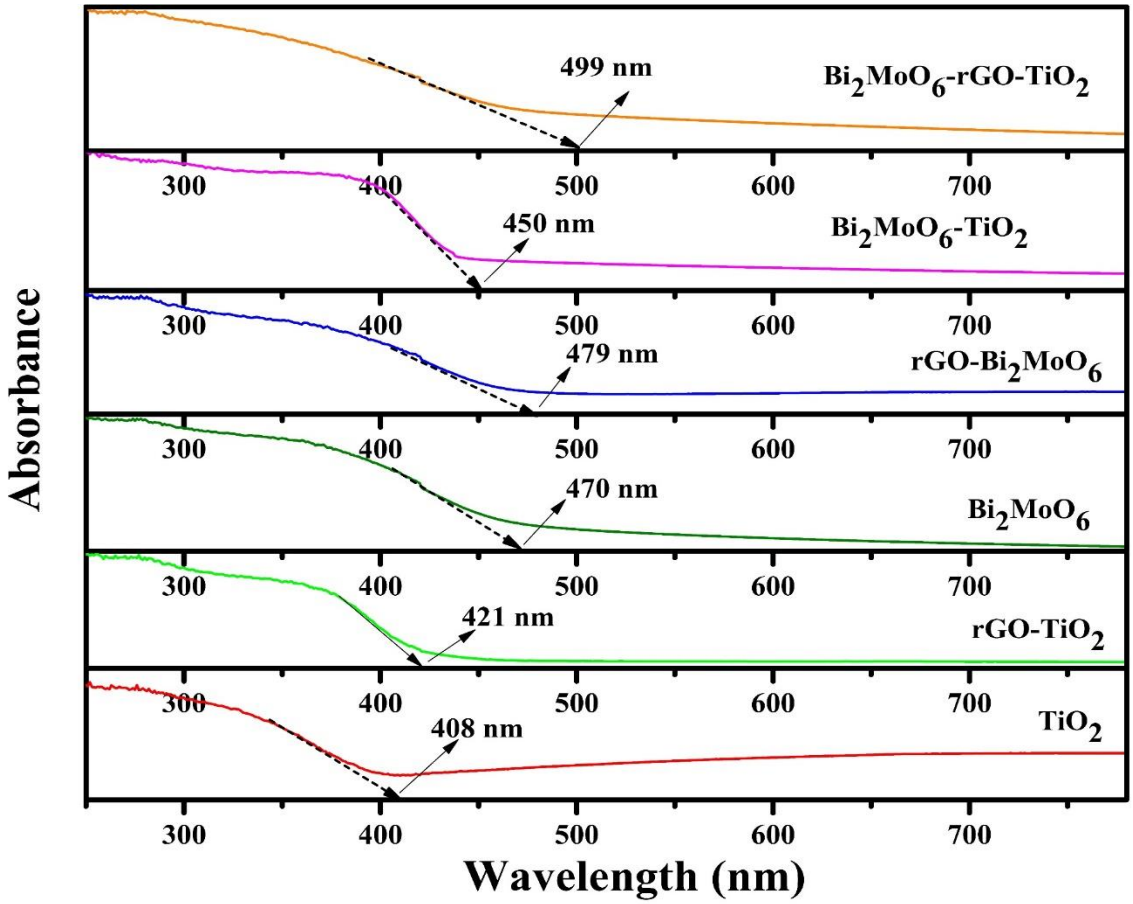

Fig.9. DRS–UV spectra of TiO_2, rGO-TiO_2, Bi_2MoO_6, rGO-Bi_2MoO_6, Bi_2MoO_6-TiO_2, and Bi_2MoO_6-rGO-TiO_2 nanocomposite

Preprints (www.preprints.org) | NOT PEER-REVIEWED | Posted: 22 February 2021 doi:10.20944/preprints202102.0495.v1

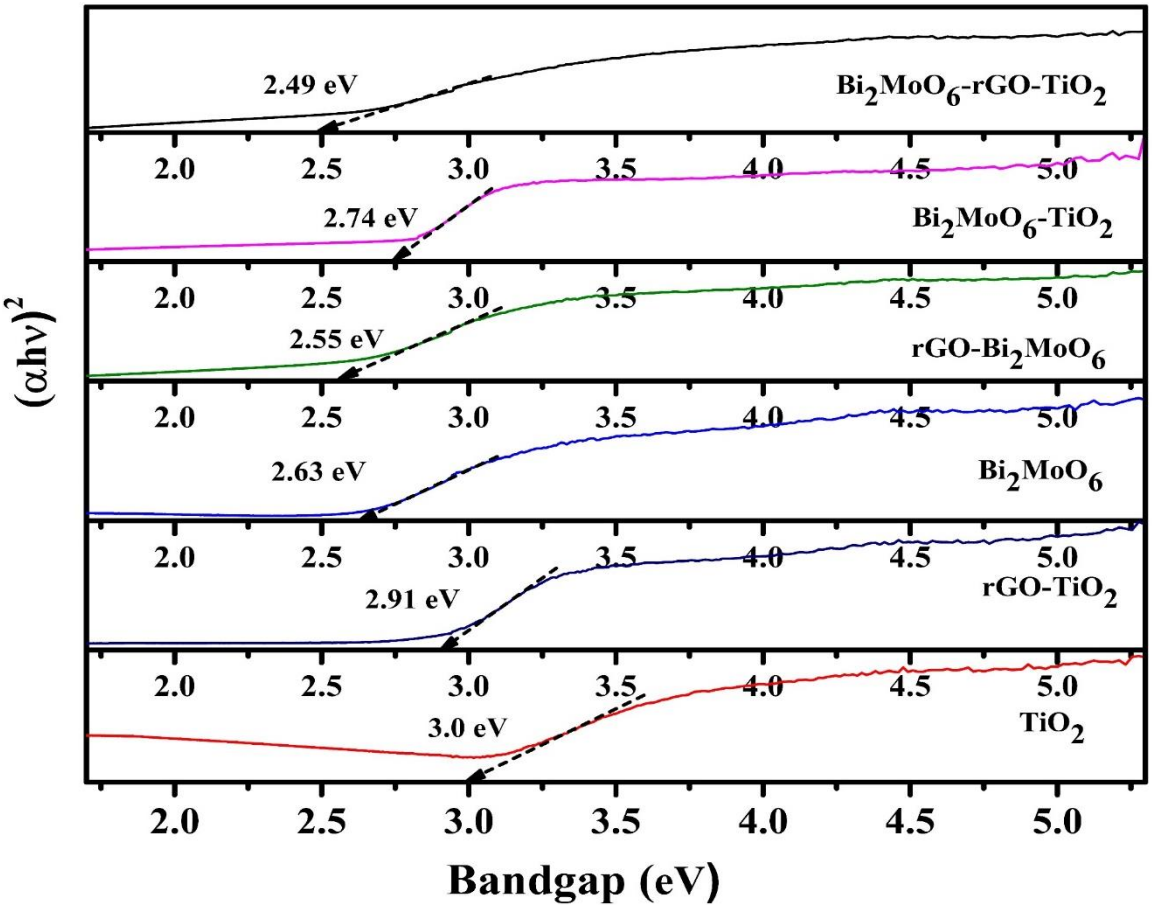

Fig.10. Kubelka–Munk function vs band gap energy (eV) of TiO_2, rGO-TiO_2, Bi_2MoO_6, rGO-Bi_2MoO_6, Bi_2MoO_6-TiO_2 and Bi_2MoO_6-rGO-TiO_2 nanocomposite

Preprints (www.preprints.org) | NOT PEER-REVIEWED | Posted: 22 February 2021 doi:10.20944/preprints202102.0495.v1

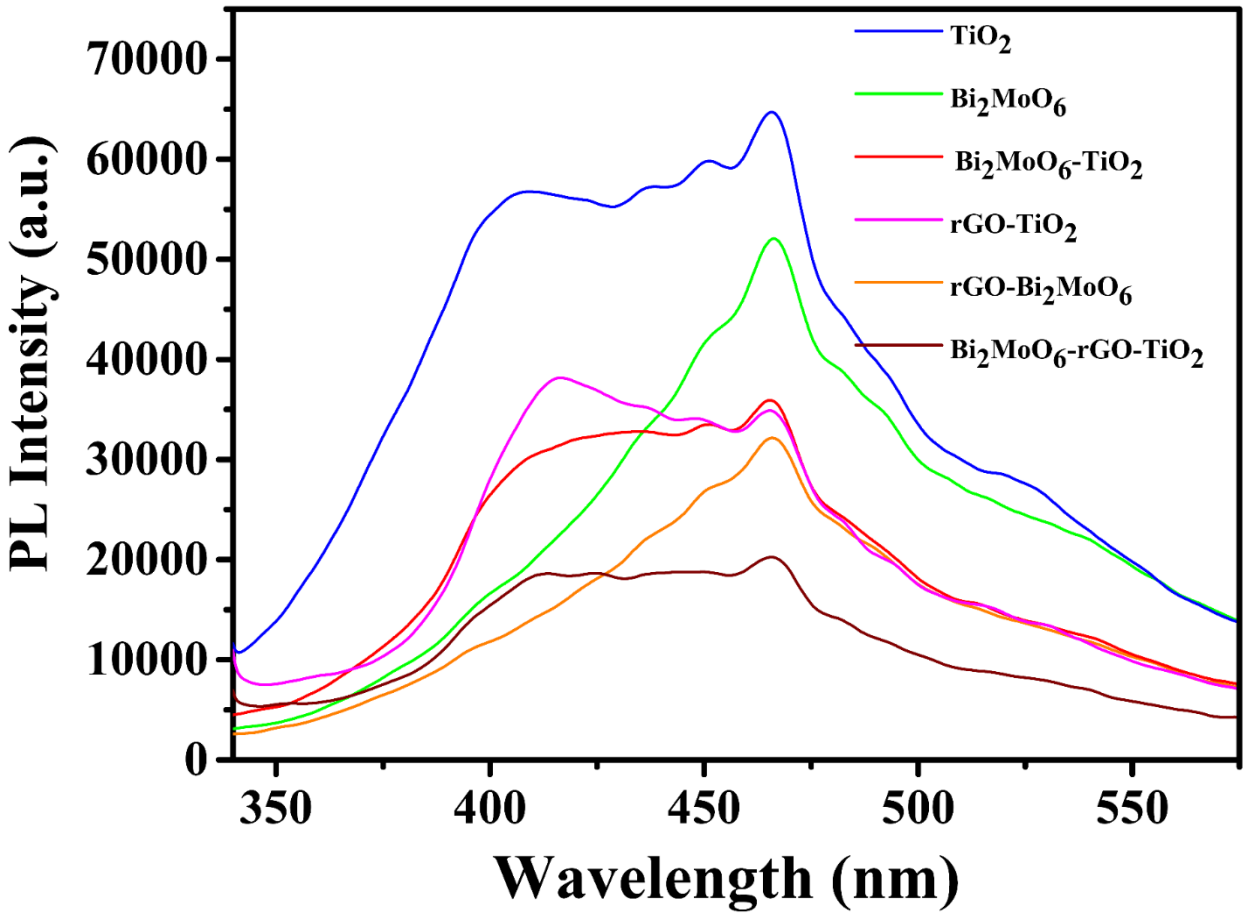

Fig.11. Photoluminescence spectra of TiO_2, Bi_2MoO_6, Bi_2MoO_6-TiO_2, rGO-TiO_2, rGO-Bi_2MoO_6, and Bi_2MoO_6-rGO-TiO_2 nanocomposite

Preprints (www.preprints.org) | NOT PEER-REVIEWED | Posted: 22 February 2021 doi:10.20944/preprints202102.0495.v1

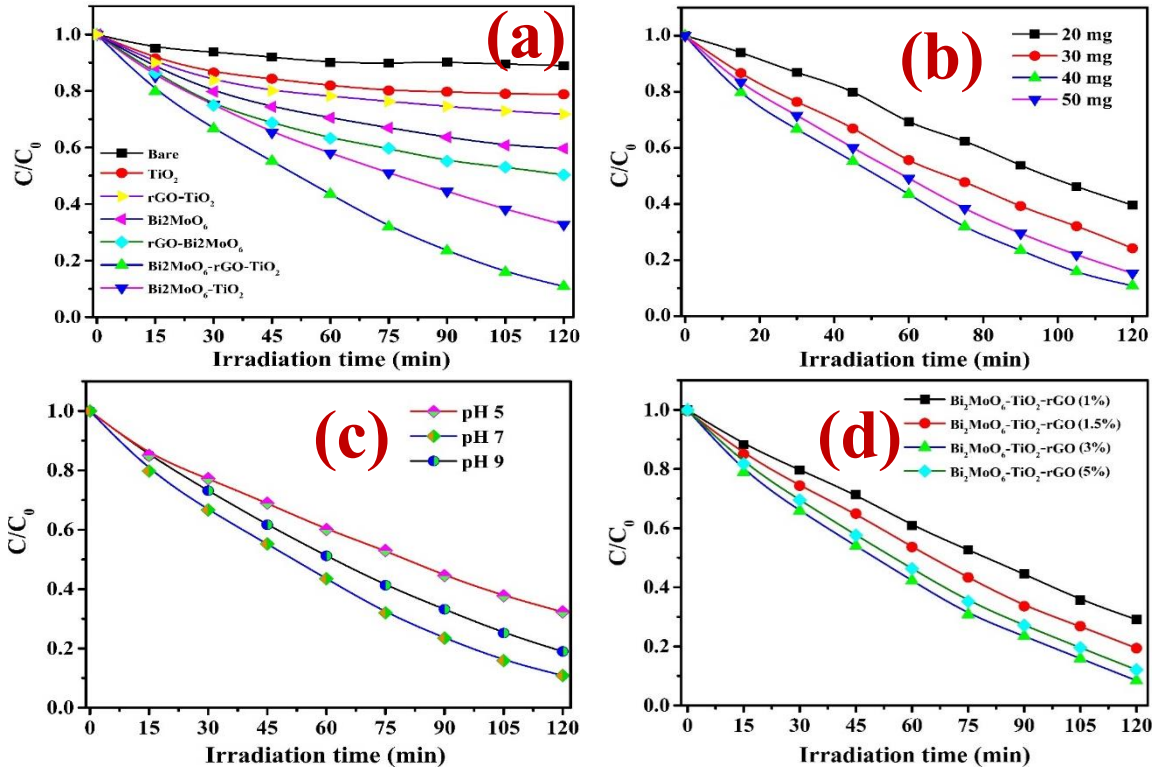

Fig. 12. Photocatalytic degradation of ofloxacin under different conditions: (a) different catalysts (catalysts: 40 mg/L, ofloxacin conc.: 4×10^{-5} M, and pH-4). (b) different weight ratio of Bi_2MoO_6-rGO-TiO_2 (ofloxacin conc.: 4×10^{-5} M), (c) different pH condition of ofloxacin in the presence of Bi_2MoO_6-rGO-TiO_2. (d) different percentages of rGO in Bi_2MoO_6-rGO-TiO_2

Preprints (www.preprints.org) | NOT PEER-REVIEWED | Posted: 22 February 2021 doi:10.20944/preprints202102.0495.v1

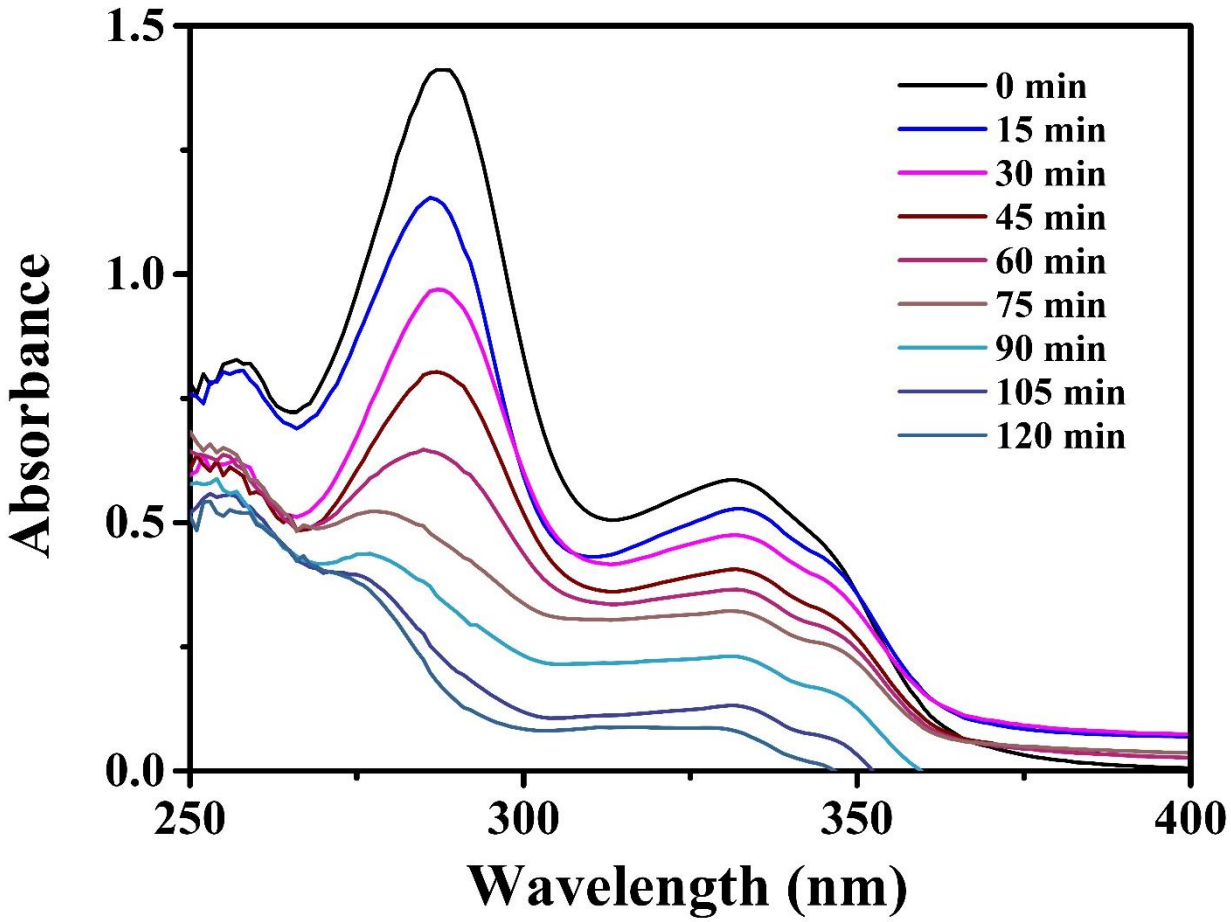

Fig.13. Absorption spectrum of photodegradation of 4×10^{-5} M conc. aqueous ofloxacin solution under visible light illumination in the presence of 40 mg of Bi_2MoO_6-rGO-TiO_2 nanocomposite at different irradiation times.

Preprints (www.preprints.org) | NOT PEER-REVIEWED | Posted: 22 February 2021 doi:10.20944/preprints202102.0495.v1

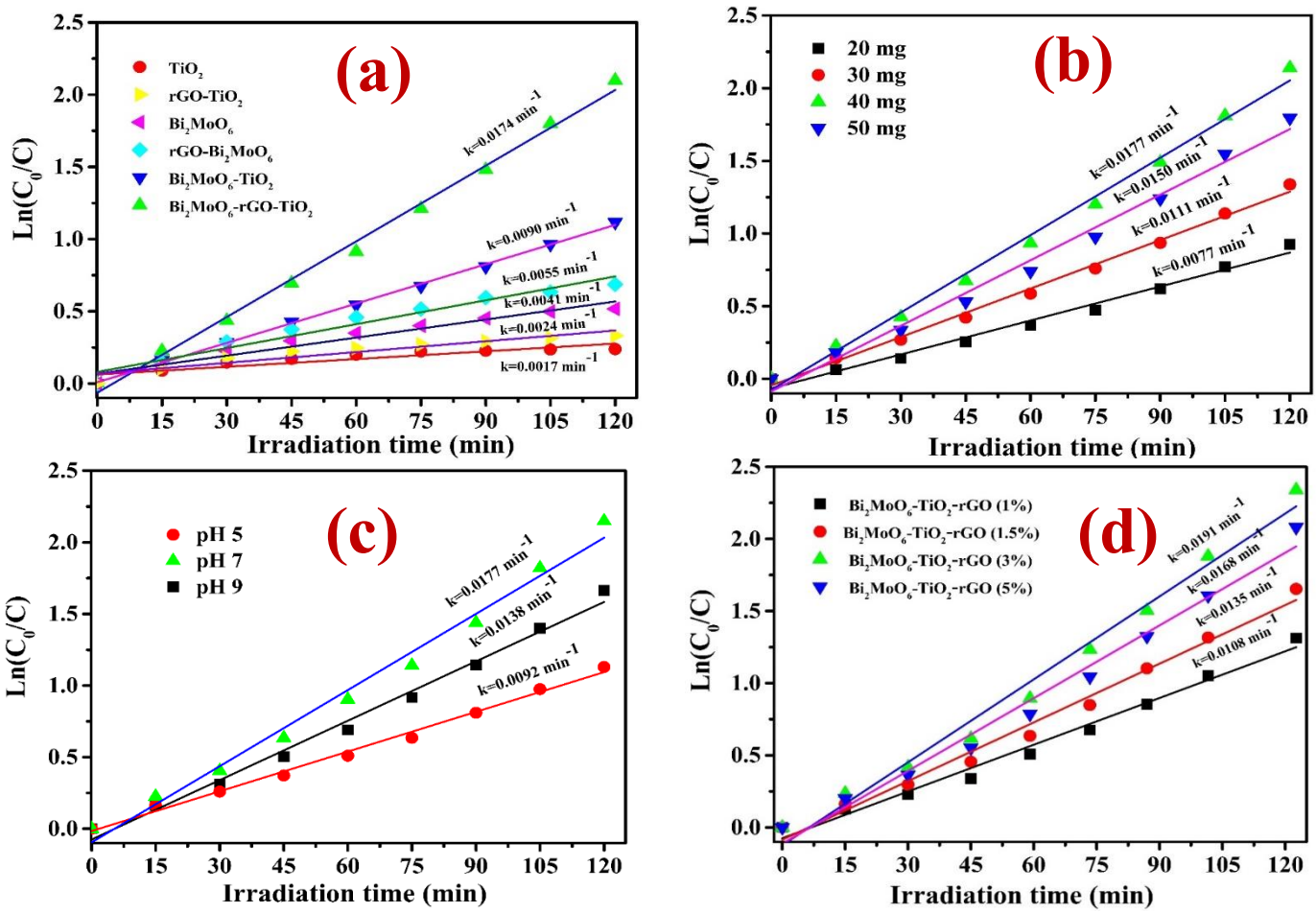

Fig. 14. (a) first-order kinetic plots of ln[C_0/C] vs time for different catalysts, (b) first-order kinetic plots of ln[C_0/C] vs time for different dosage of catalyst (c) first-order kinetic plots of ln[C_0/C] vs time for different pH of ofloxacin in the presence of Bi_2MoO_6-rGO-TiO_2 (d) first-order kinetic plots of ln[C_0/C] vs time for different percentages of rGO in Bi_2MoO_6-rGO-TiO_2

Preprints (www.preprints.org) | NOT PEER-REVIEWED | Posted: 22 February 2021 doi:10.20944/preprints202102.0495.v1

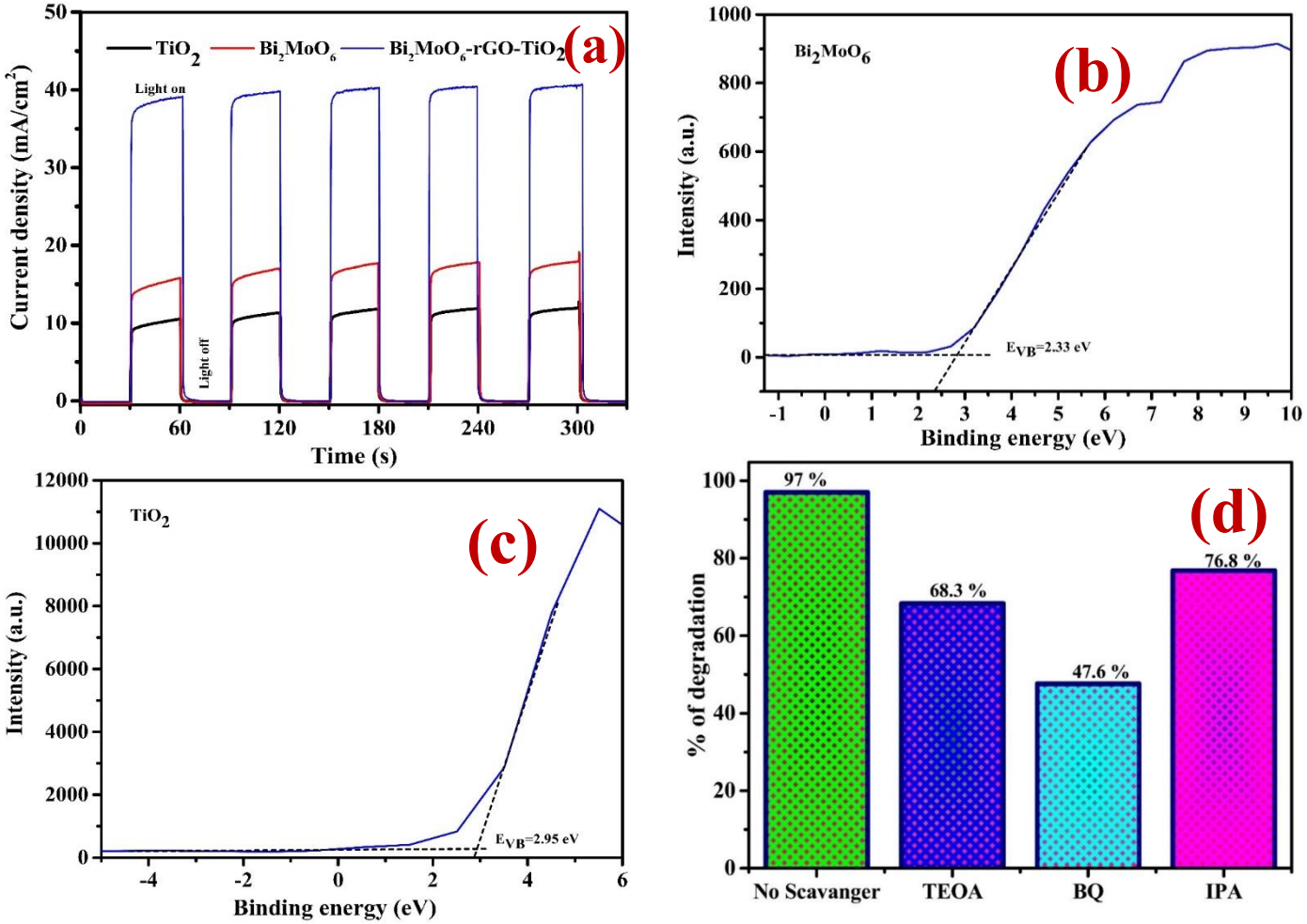

Fig. 15. (a) Photocurrent densities of TiO_2, Bi_2MoO_6 and Bi_2MoO_6-rGO-TiO_2, (b, c) XPS valance spectra of TiO_2 and Bi_2MoO_6, (d) Percentage of photocatalytic reduction of ofloxacin with Bi_2MoO_6-rGO-TiO_2 in the presence of different scavengers (ofloxacin conc.: 4×10^{-4} M; Bi_2MoO_6-rGO-TiO_2 -40 mg; TEOA- 1 mmol in 100 mL/BQ-0.01 mmol in 100 mL/IPA-0.1 mmol in 100 mL, irradiation time at 120 min)

Preprints (www.preprints.org) | NOT PEER-REVIEWED | Posted: 22 February 2021 doi:10.20944/preprints202102.0495.v1

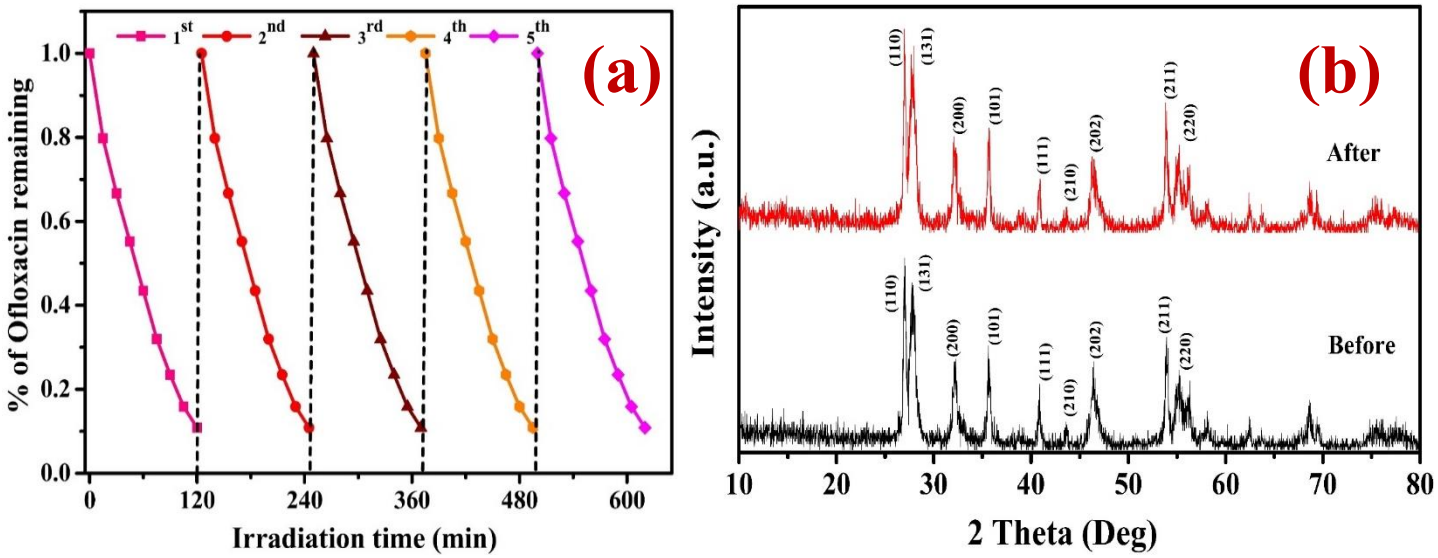

Fig. 16. (a) Recycle efficiency of photocatalyst for 5 cycles, (b) X-ray diffraction spectra for Bi_2MoO_6-rGO-TiO_2 before and after degradation of ofloxacin

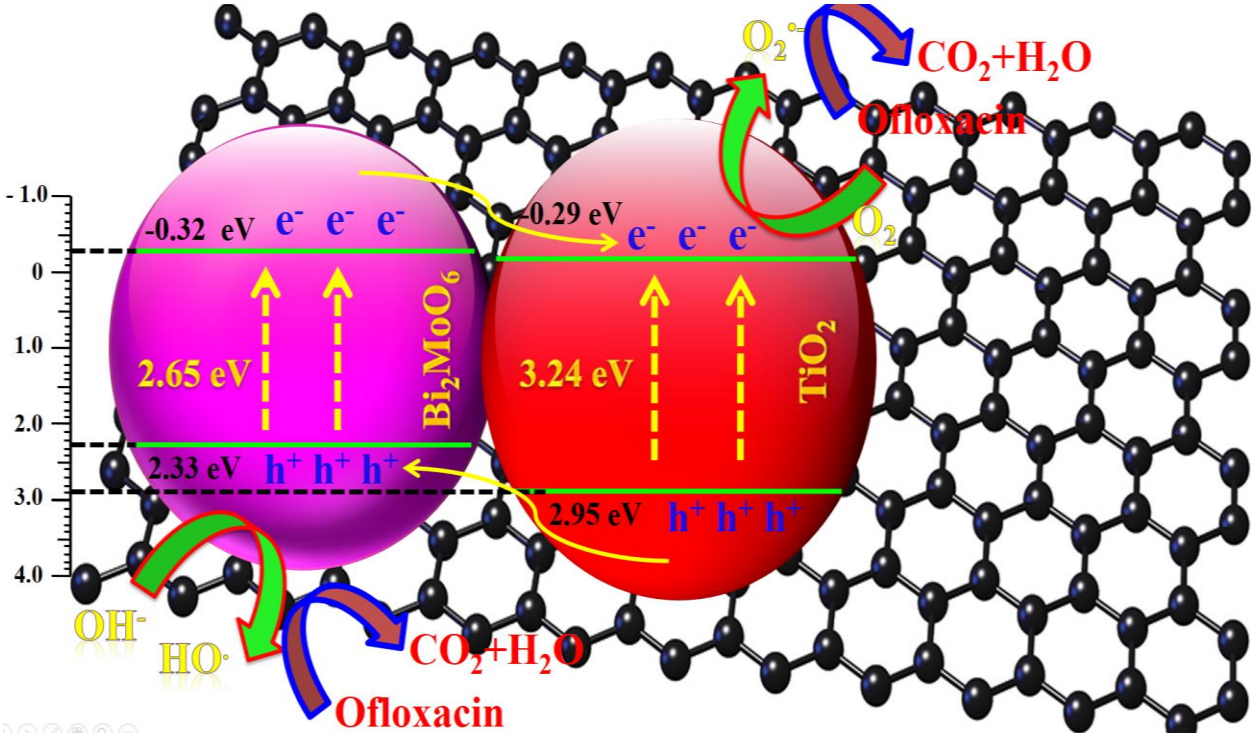

Scheme 1

Table 1

Preprints (www.preprints.org) | NOT PEER-REVIEWED | Posted: 22 February 2021 doi:10.20944/preprints202102.0495.v1

Table 1

S.No	Photocatalyst	Organic pollutant	Light source	pH	Catalyst dosage (mg/L)	Degradation time (min)	Degradation percentage (%)	Ref.
1	Bi_2MoO_6	Ofloxacin	Visible light	7	50	240	90	[77]
2	ZnO/Bi_2MoO_6	Ofloxacin	Visible light	7	50	240	100	[78]
3	Zeolite-Boron-TiO_2	Ofloxacin	UV-Light	-	20	240	98	[79]
4	BiOCl/BiOBr–$Bi_{24}O_{31}Br_{10}$	Ofloxacin	Solar light	6	200	180	78	[80]
5	$Sm_2Ti_2O_7$/1HZSM-5	Ofloxacin	UV-Light	-	30	150	93.5	[81]
6	CdS/TiO_2	Ofloxacin	Visible light	9	450	180	86	[82]
7	Bi_2MoO_6	Ofloxacin	Solar light	6	1000	90	70	[83]
8	ZnO/CdS	Ofloxacin	Visible light	7	50	240	90	[84]
9	Bi_2MoO_6-rGO-TiO_2	Ofloxacin	Visible light	7	40	120	92.3	This work